AGU PUBLICATIONS

JGR

Journal of Geophysical Research: Earth Surface

RESEARCH ARTICLE
10.1002/2015JF003760

Key Points:
- Wilkes Subglacial Basin (WSB) sedimentary basins are characterized for the first time
- North and south WSB sedimentary subbasin distribution and isopachs are significantly dissimilar
- Variation in WSB subglacial sediment distribution and character suggests disparate glacial history

Correspondence to:
B. C. Frederick,
bruce.c.frederick@gmail.com

Citation:
Frederick, B. C., D. A. Young, D. D. Blankenship, T. G. Richter, S. D. Kempf, F. Ferraccioli, and M. J. Siegert (2016), Distribution of subglacial sediments across the Wilkes Subglacial Basin, East Antarctica, *J. Geophys. Res. Earth Surf.*, *121*, 790–813, doi:10.1002/2015JF003760.

Received 12 OCT 2015
Accepted 7 APR 2016
Accepted article online 11 APR 2016
Published online 29 APR 2016

Distribution of subglacial sediments across the Wilkes Subglacial Basin, East Antarctica

Bruce C. Frederick[1], Duncan A. Young[2], Donald D. Blankenship[2], Thomas G. Richter[2], Scott D. Kempf[2], Fausto Ferraccioli[3], and Martin J. Siegert[4]

[1]Department of Geology, University of Kansas, Lawrence, Kansas, United States, [2]Institute for Geophysics, Jackson School of Geosciences, University of Texas at Austin, Austin, Texas, United States, [3]British Antarctic Survey, Cambridge, UK, [4]Grantham Institute, Department of Earth Sciences and Engineering, Imperial College, London, UK

Abstract Topography, sediment distribution, and heat flux are all key boundary conditions governing the dynamics of the East Antarctic Ice Sheet (EAIS). EAIS stability is most at risk in Wilkes Land across vast expanses of marine-based catchments including the 1400 km × 600 km expanse of the Wilkes Subglacial Basin (WSB) region. Data from a recent regional aerogeophysical survey (Investigating the Cryospheric Evolution of the Central Antarctic Plate (ICECAP)/IceBridge) are combined with two historical surveys (Wilkes basin/Transantarctic Mountains System Exploration-Ice-house Earth: Stability or DYNamism? (WISE-ISODYN) and Wilkes Land Transect (WLK)) to improve our understanding of the vast subglacial sedimentary basins impacting WSB ice flow and geomorphology across geologic time. Analyzing a combination of gravity, magnetic and ice-penetrating radar data, we present the first detailed subglacial sedimentary basin model for the WSB that defines distinct northern and southern subbasin isopachs with average sedimentary basin thicknesses of 1144 m ± 179 m and 1623 m ± 254 m, respectively. Notably, more substantial southern subbasin sedimentary deposition in the WSB interior supports a regional Wilkes Land hypothesis that basin-scale ice flow and associated glacial erosion is dictated by tectonic basement structure and the inherited geomorphology of preglacial fluvial networks. Orbital, temperate/polythermal glacial cycles emanating from adjacent alpine highlands during the early Miocene to late Oligocene likely preserved critical paleoclimatic data in subglacial sedimentary strata. Substantially thinner northern WSB subglacial sedimentary deposits are generally restricted to fault-controlled, channelized basins leading to prominent outlet glacier catchments suggesting a more dynamic EAIS during the Pliocene.

1. Introduction

The heterogenetic distribution and character of subglacial sedimentary basin deposits have long been identified as a key constraint dictating basal ice dynamics [*Blankenship et al*., 1986; *Alley et al*., 1987]. Here we introduce the first sedimentary basin isopachs for the entire Wilkes Subglacial Basin (WSB), an approximate 700,000 km^2 expanse immediately west of the Transantarctic Mountain (TAM) range with an average bed elevation of 500 m below sea level [*Drewry*, 1983] and eustatic sea level rise potential estimated at 3–7 m [*Mengel and Levermann*, 2014; *Pollard et al*., 2015]. Basal constraints presented herein quantify sedimentary basin distribution, thickness, and lithologic character and provide insight into the geomorphologic history of the basin while standing to improve the accurate parameterization of future basal hydraulic, geothermal flux, and ice dynamic models in the region (Figure 1).

While the existence of a sediment-draped WSB was first postulated as early as the 1970s from airborne ice-penetrating radar data [*Drewry*, 1976], the tectonic evolution of the basin remains controversial. Mutually incompatible structural models have been suggested including a flexural downwarp of lithosphere [*Stern and ten Brink*, 1989], a rift basin scenario [*Steed*, 1983], and most recently, a region of extended terrain with amagmatic, Cenozoic denudation [*Ferraccioli et al*., 2009; *Jordan et al*., 2013]. Regardless of the tectonic forcing mechanism, Eocene to early Oligocene fluvial denudation, subsequent temperate\polythermal glacial scouring processes across the early Miocene, and the establishment of a stable polar ice sheet by the middle Miocene would have dominated geomorphologic evolution of the WSB following the proximal TAM uplift in the Cretaceous [*Sugden et al*., 1995; *Stern et al*., 2005; *Lawrence et al*., 2007]. Despite historical viewpoints that the East Antarctic Ice Sheet (EAIS) has been relatively stable compared to the West Antarctic Ice Sheet [*Mercer*, 1978], more recent Wilkes Land studies have suggested that the EAIS (particularly where grounded below

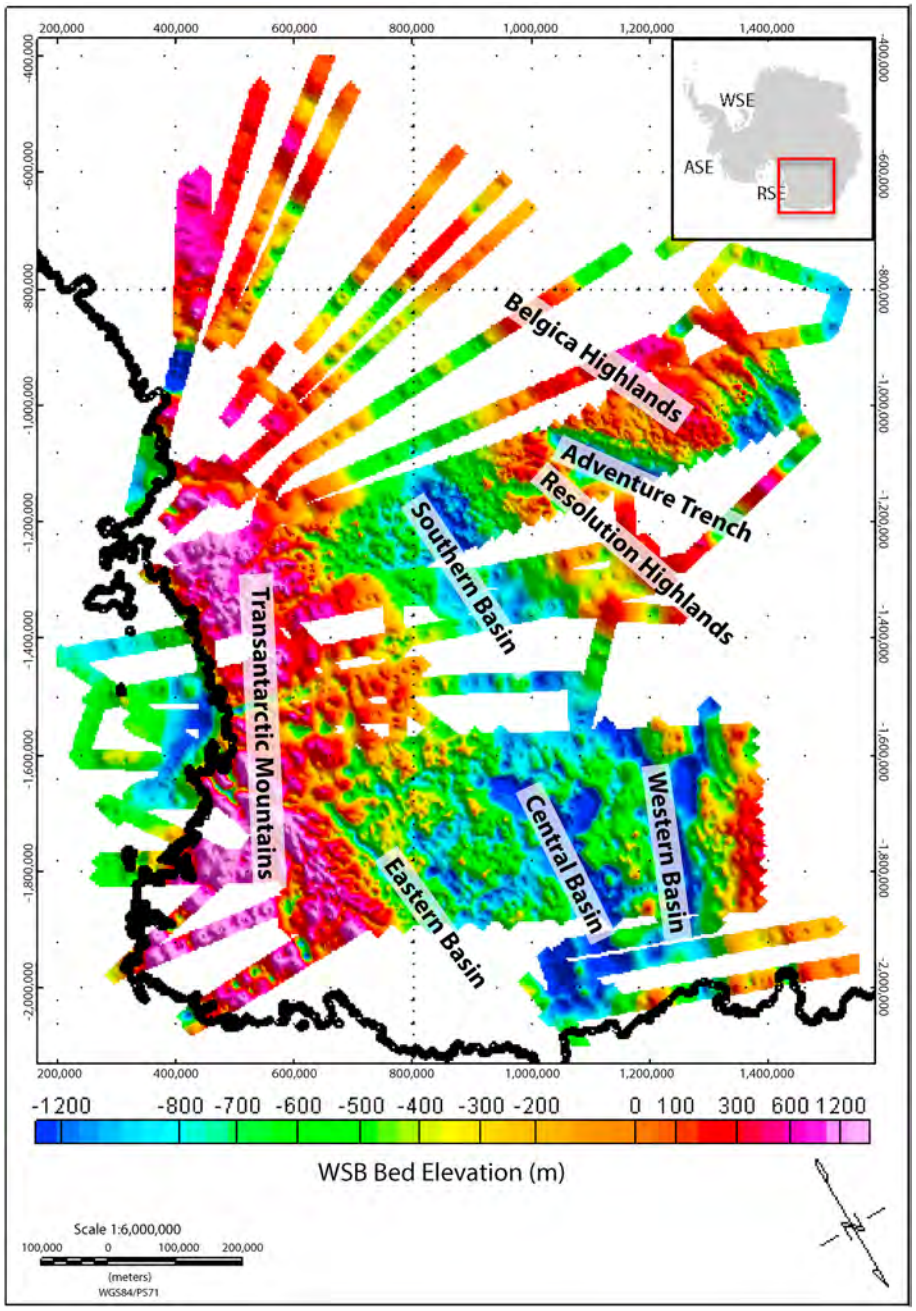

Figure 1. Wilkes Subglacial Basin subglacial bed topography with subglacial subbasins and highlands labeled. Aerogeophysical sounding data presented as meters relative to WGS-84 and gridded at 2 km using a minimum curvature approach.

current sea level) has been cyclically dynamic across more finite timescales (10^4–10^5 years) than previously suspected [*Young et al.*, 2011; *Cook et al.*, 2013; *Mengel and Levermann*, 2014].

Such glacial modulation across the WSB for millennia would have not only served to promote the bed-depression overdeepening and interior-sloping basin floors characterizing the present-day WSB but would also erode, transport, and deposit gigatons sediment leading to reductions in topographic relief and effective stress with corresponding increases in subglacial basal till deformation, shear, and faster ice flow [*Alley et al.*, 1987; *Blankenship et al.*, 1986]. Ice sheet insulation combined with regional geothermal heat flux estimates on the order of 50 mW m^{-2} [*Siegert and Dowdeswell*, 1996; *Nyblade*, 1999; *Wright and Siegert*, 2012] predicts a wealth of subglacial water systems, which have been identified in the Wilkes Subglacial Basin by airborne

Table 1. Aerogeophysical Equipment and Platform Specifications[a]

Campaign	Platform	Radar	Gravity	Magnetics
WLK (UTIG/LDEO; 1999–2000)[b]	Twin Otter (speed 65 m/s)	UT/TUD 60 MHz (4 MHz bandwidth)	Bell BGM-3	Geometrics 823A cesium vapor (trailing bird)
WISE-ISODYN (BAS/PNRA; 2005–2006)[c]	Twin Otter (speed 65 m/s)	PASIN 150 MHz (12 MHz bandwidth)	ZLS (S-83)	Scintrex CS3 cesium vapor (wing tip)
ICECAP (UTIG/NERC/IceBridge; 2008–2011)[d]	Basler BT-67 (speed 90 m/s)	HiCARS 60 MHz (15 MHz bandwidth)	Bell BGM-3	Geometrics 823A cesium vapor (tail boom)

[a]BAS: British Antarctic Survey, LDEO: Lamont Doherty Earth Observatory, PNRA: Italian Programma Nazionale di Ricerche in Antartide, and UTIG: University of Texas Institute for Geophysics.
[b]http://www-udc.ig.utexas.edu/external/facilities/aero/data/soar/WLK/SOAR_wlk.htm.
[c]https://secure.antarctica.ac.uk/data/aerogeo/access/wise/.
[d]https://nsidc.org/data/icebridge/data_summaries.html.

radar and satellite remote sensing [*Wingham et al*., 2006; *Carter et al*., 2007; *Smith et al*., 2009; *McMillan et al*., 2013; *Wright et al*., 2014]. Sediments play an important role in shaping subglacial water systems, as demonstrated by the discovery of vast systems of canals in deformable sediment underlying Thwaites Glacier in West Antarctica [*Schroeder et al*., 2013, 2014]. In that case, the sediment-floored canals reduced basal drag in comparison with sediment starved, concentrated subglacial channel systems downstream in a region of increased basal drag, greater scouring, and erosion.

In this study, we provide the first quantitative estimates for extent, thickness, and character of WSB sedimentary basin deposits lying beneath the EAIS. To evaluate subglacial sedimentary basin boundaries, area, volume, and potential depositional controls, we integrate over 110,867 line kilometers of aerogeophysical data collected as part of NASA's IceBridge program and the University of Texas-Austin Institute for Geophysics (UTIG) ICECAP (Investigating the Cryospheric Evolution of the Central Antarctic Plate) program across four austral field seasons between 2008 and 2013, combined with historical WSB aerogeophysical data flown during the WISE (Wilkes basin/Transantarctic Mountains System Exploration)-ISODYN (Ice-house Earth: Stability or DYNamism?) campaign of 2005–2006 [*Ferraccioli et al*., 2009; *Jordan et al*., 2013] and the WLK (Wilkes Land Transect) campaign of 1999–2000 [*Studinger et al*., 2004; *Carter et al*., 2009].

2. Data Recovery and Preprocessing

Aerogeophysical platforms and equipment varied across field seasons as detailed in Table 1. The UTIG ICECAP aerogeophysical surveys maintained consistent instrumentation and processing techniques throughout the four seasons of data used here. ICECAP flight profiles were designed in a radial pattern extending from the sea ice runway at McMurdo into the interior of the Southern Wilkes Basin in order to maximize the total aerogeophysical coverage area and cross-historical airborne surveys wherever possible. IceBridge aerogeophysical flight line data, collected along historical ICESat satellite survey tracks, have been incorporated into the data here where applicable.

Additional instrument altitude constraints were incorporated into flight survey design. While airborne gravimeters perform best when flying at a constant altitude, the 60 MHz ice-penetrating radar returns are significantly attenuated at altitudes exceeding 1000 m above the ice surface. Due to these instrumentation constraints and an ice surface relief exceeding 2500 m over the survey area, radial aerogeophysical survey flight paths were often flown at several consistent altitudes in a stair-stepped vertical profile. To help mitigate large aircraft acceleration impacts on the gravimeter, smooth altitude changes were generally performed over a distance of 25–35 km. The Bell BGM-3 gravimeter samples every 1 Hz (approximately every 90 m along track at Basler BT-67 airspeeds), an estimated precision of less than 3 mGal, and concurrent dual frequency carrier phase GPS data separately recorded at 0.1 m resolution for subsequent use in gravity data processing. The Geometrics 823A cesium vapor magnetometer was towed behind the aircraft in a 3 m tail boom to achieve a better than 1 nT precision and a track line sampling distance of approximately 9 m. Topographic surface data were collected with a fixed, nadir-pointing laser altimeter allowing for 2-D reconstruction of the ice surface elevation to within 0.25 m accuracy and an along-track sampling distance of 10 m. Ice-penetrating radar data were collected using a High Capability Radar Sounder

(HiCARS) with a 60 MHz center frequency and 15 MHz bandwidth. Ice thickness estimates were obtained using coherent, synthetic aperture radar with a track line sampling distance every 25 m.

2.1. Gravity Reduction

Gravity data reduction and preprocessing for the ICECAP data was performed in accordance with methodologies developed and detailed in *Holt et al*. [2006] and *Richter et al*. [2001]. Raw gravity data from the BGM-3 were mapped with concurrent GPS data, time stamped, and then corrected for vertical or horizontal aircraft acceleration, yaw, pitch, and roll. An Eötvös correction was then applied to account for the acceleration resulting from the Earth's rotation relative to WGS-84 such that the gravity meter and the source are vertically aligned. Data were smoothed with a finite impulse response low-pass filter with a half-amplitude frequency point of 0.0054 Hz (185 s) resulting in an estimated spatial resolution of 7.9 km. The gravity signal was then corrected for aircraft altitude using the theoretical spheroid gravity algorithm developed by *Featherstone* [1995]. Final edits of the preprocessed gravity results were completed by crossover error assessment, visual analysis of the plotted data, and root-mean-square (RMS) analysis. Often the beginning of a line had to be trimmed to reduce the RMS, or in some cases, entire lines had to be removed from the data set because of excessive in-flight turbulence.

The resultant free-air gravity disturbance for each survey across the WSB was leveled to a consistent data elevation of 3950 m above the ellipsoid, to correspond to the highest aircraft altitude flown during the composite WSB aerogeophysical surveys, to provide consistent spectral content for subsequent power spectra analysis using Generic Mapping Tools (GMT) [*Wessel and Smith*, 1998]. At the 3950 m upward continued elevation, the closest bedrock sources would yield an expected resolvable geologic wavelength of ~6.5 km for ideal flight conditions based upon calculations for different basin widths using formulas developed by *Childers et al*. [1999]. Gravity measurements for the ICECAP/IceBridge and WLK surveys were tied to the International Gravity Standardization Network (IGSN-71) at McMurdo Station, while the WISE-ISODYN gravity data set was linked to the IGSN-71 at Mario Zucchelli Station. Following leveling and upward continuation, RMS crossover errors were calculated at profile intersections and an appropriate DC shift applied to survey profiles to match consistent downward continued free-air gravity anomalies derived from the gravity field and steady state Ocean Circulation Explorer (GOCE) satellite global data field. Crossover errors were minimized to less than 3 mGal with an estimated horizontal spatial resolution of 9 km. Resultant upward continued free-air gravity data sets were then gridded separately at 2 km using a minimum curvature approach, sutured together, and plotted (Figure 2) using Geosoft's Oasis montaj® software suite.

2.2. Magnetics Reduction

Aeromagnetic data were processed using standard methodologies including diurnal and International Geomagnetic Reference Field (IGRF) corrections followed by subsequent leveling to minimize cross-line differences. While the IGRF model details very long wavelength and scale variations in the Earth's magnetic field, and diurnal variations in the Earth's magnetic field occur across much more finite (daily) time intervals, it should be noted that neither magnetic data reduction technique can fully account for magnetic measurement variability across a 4 year aerogeophysical program. Persistent variability in cross-line differences in the magnetic data set may be the result of flight altitude differences, equipment configuration changes between field seasons, or imperfect removal of the diurnal field [*Minty*, 1991]. Despite complex line-tie line geometries arising from the unusual design of the ICECAP/IceBridge surveys, basic statistical leveling techniques were able to be employed using Geosoft's Oasis montaj® software suite with sufficient accuracy for a regional survey model of this scale. Geosoft's Oasis montaj® software aeromagnetic data leveling algorithms calculate a least squares trend line to derive a trend error curve that is subsequently added to the channel to be leveled. Once leveled, magnetic data were gridded using a minimum curvature method with a cell size of 2 km, draped on the composite Bedmap2 [*Fretwell et al*., 2013] bed topography at an altitude of 3950 m, and displayed in Figure 3 with individual data sets sutured into a single composite grid using Geosoft's Oasis montaj® software GridKnit extension.

Leveled aeromagnetic data draped to the subglacial topographic bed surface and upward continued to an elevation of 3950 m was utilized to define regional faults across the WSB (Figure 3) to gain a better understanding of potential lithologies and associated lithologic densities that might laterally constrain

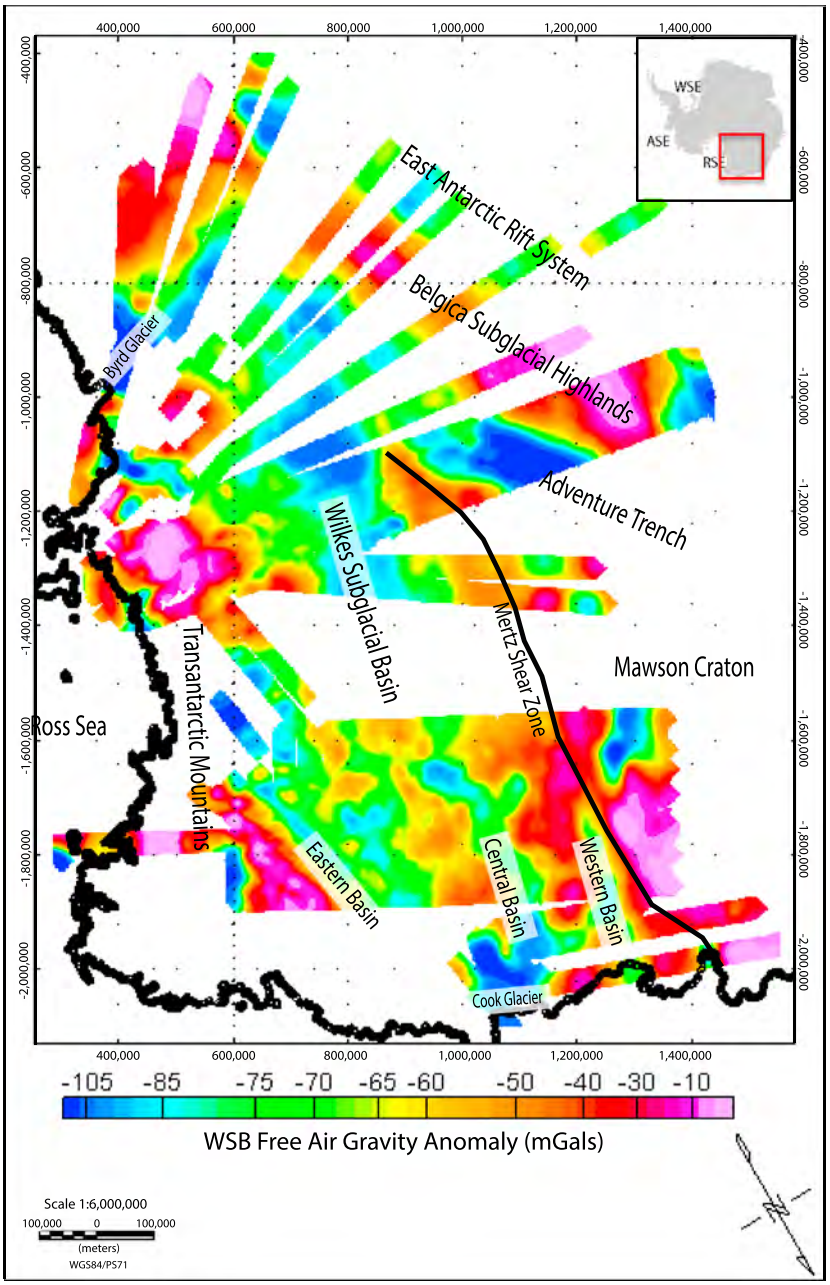

Figure 2. Wilkes Subglacial Basin Free-Air Gravity (mGal) ICECAP/IceBridge, WLK, and WISE-ISODYN data sets leveled to 3950 m in a Polar Stereographic 71 (PS71) projection. The topographic bias inherent to free-air anomalies is apparent with subglacial basins appearing blue green.

sedimentary deposition and facies. Regional faults were identified based on conjugate margin structural reconstruction by *Aitken et al.* [2014] and structural interpretation of the northern WSB following the WISE-ISODYN aerogeophysical survey by *Ferraccioli et al.* [2009].

2.3. Radar Reduction

Airborne ice-penetrating radar data from multiple surveys were pulse compressed, processed using a short synthetic aperture radar aperture to retain energy, and compiled regionally to achieve range distortions below 400 m. Ice thicknesses were calculated assuming a radio wave speed in ice of 169 m/μs^{-1}, and the bed elevation calculated relative to the coincident surface reflections. Bedmap2 digital elevation models

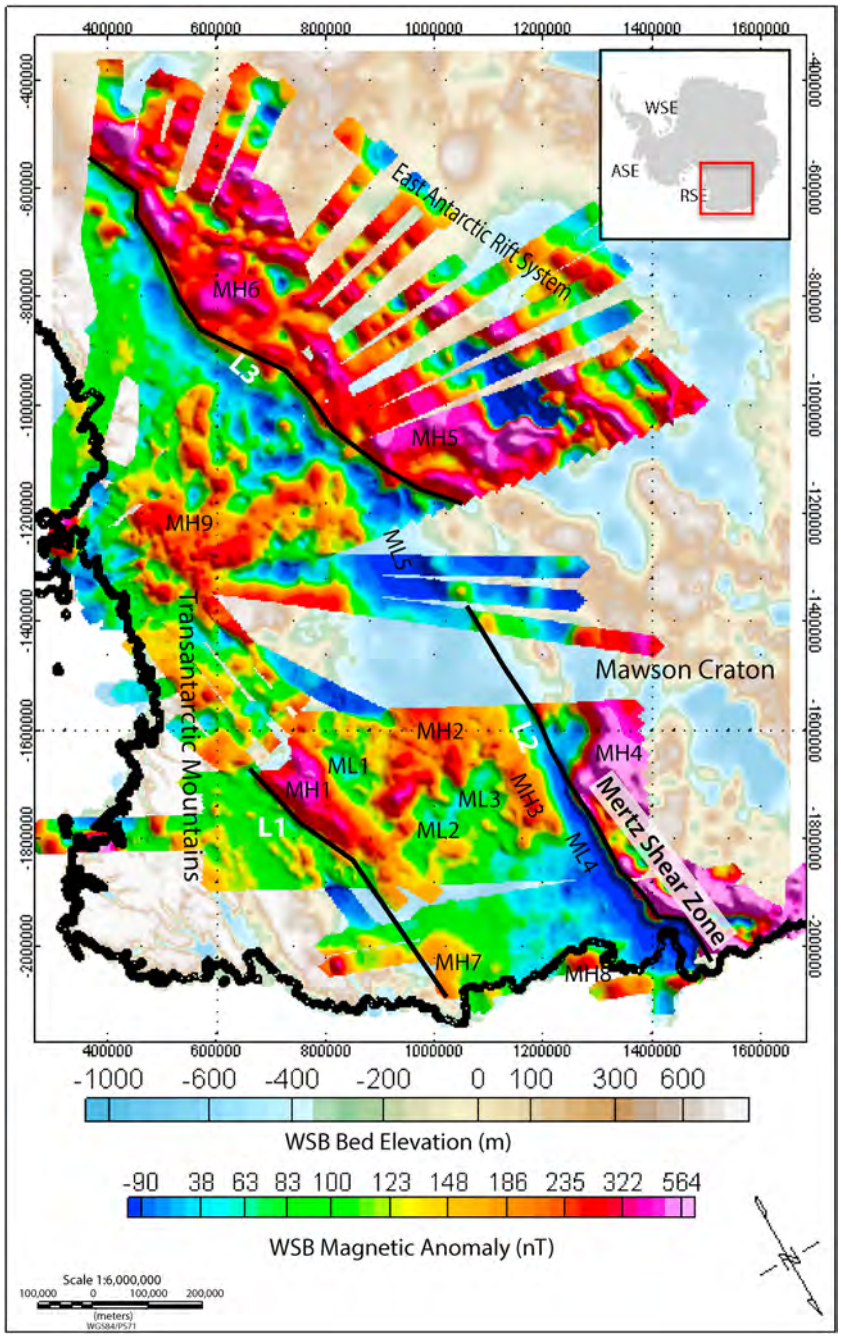

Figure 3. Wilkes Subglacial Basin magnetic data anomaly map compiled from ICECAP/IceBridge, WLK, and WISE-ISODYN surveys draped on the composite Bedmap2 bed topography at an altitude of 3950 m [*Fretwell et al.*, 2013]. Major aeromagnetic high and low anomalies (MH1–MH9 and ML1–ML5), faults, and lineaments (L1–L3) have been labeled consistent with *Ferraccioli et al.* [2009] and *Jordan et al.* [2013] indicating potential structural constraints to basin evolution.

for ice surface and bed topography [*Fretwell et al.*, 2013] were augmented with ice-penetrating radar data collected during ICECAP/IceBridge field seasons 2010–2013. The latest ice and bed digital elevation surfaces attained from ICECAP/IceBridge radar ice thickness data were gridded at a spacing of 5 km and sutured to regional Bedmap2 ice surface and bed topography data using Geosoft's Oasis montaj® Gridknit extension. The updated Bedmap2 ice surface and bed elevation data sets were then interpolated using a natural neighbor algorithm [*Watson*, 1992] at a cell size of 5 km to facilitate incorporation into 3-D cryospheric-lithospheric density model for subsequent gravity reduction.

3. Geophysical Analysis and Modeling

3.1. Bouguer Anomaly Estimation

The Bouguer anomaly maps out the density variations not due to known topographic loads. Complete terrain-corrected Bouguer gravity anomalies were derived using a Parker-Oldenberg approach [*Parker*, 1973; *Oldenburg*, 1974] included as part of Geosoft's Oasis montaj® software suite. The Parker-Oldenberg algorithms, estimate the gravitational effects of topography using *LaFehr's* [1991] curvature correction with intermediate zones (one to eight grid cells from the gravity station) calculated using the flat-topped square prism approach [*Nagy*, 1966], and the far zone (>8 grid cells from the gravity station) terrain effect calculated using the annular ring segment approximation of [*Kane*, 1962]. Incorporating airborne radar data from the ICECAP, WLK, and WISE-ISODYN surveys, the 3-D gravitational effect of the ice sheet and bed topography was calculated at an altitude of 3950 m using average ice and bedrock densities of 0.92 g/cm^3 and 2.67 g/cm^3 [*Studinger et al*., 2004; *Filina et al*., 2006; *Jordan et al*., 2013], respectively. Subtracting these calculated gravity effects from the free-air anomaly yielded the full terrain-corrected Bouguer gravity results gridded and displayed in Figure 4 with similar resolution and gridding techniques used for free-air gravity results. These resultant Bouguer gravity anomalies do not reflect data over floating ice, as water depths were not adequately constrained and potential Bouguer data along the continental margin was not required in construction of an interior WSB sedimentary basin model.

3.2. Free-Air Gravity Spectral Analysis

As the frequency content of a potential field changes with distance from the source, we can use the spectral content of our potential field data to estimate depth to major crust and near-surface density boundaries [*Spector and Grant*, 1970]. Spectral analyses of free-air gravity data were thereby assessed in areas of relatively homogeneous crustal structure, so slope breaks indicative of a change in spectral power could be easily identified. Finite gridded areas (200 km × 200 km) of free-air gravity data were selected in the southern and northern WSB, respectively, and the data mirrored along two axes to generate 800 km × 800 km grids to improve the recovery of longer wavelength signals [*McNutt*, 1983]. Data gaps were interpolated using minimum curvature to reduce potential ringing associated with data line truncations. The larger mirrored analysis area allowed for spectral depth estimates down to an upper resolution limit of 67 km with less than 10% error [*Regan and Hinze*, 1976]. Lower resolution limits for the WSB free-air gravity power spectra were also estimated at 0.1111 km^{-1} (9 km). This methodology was based upon prior potential field analytics established by *Damiani et al*. [2014], *Fairhead and Okereke* [1988], and *Karner and Watts* [1983].

The radial power spectrum of the free-air gravitational response was plotted as the natural log of power versus wave number. Least squares line segments were fit to slope breaks to determine representative crustal density boundary depths using the equation

$$h = -s/4\pi \tag{1}$$

where h = depth to source and s = slope of the (natural log) energy spectrum (Figure 5).

With each resultant slope indicative of the characteristic power spectrum, breaks in slope identify a density change at a boundary of specified wavelength or wave number [*Spector and Grant*, 1970; *Damiani et al*., 2014].

Depth estimate-wave number correlations confirm lithospheric sources at the ice-sediment, sediment-crust, and crust-mantle interfaces for the Ross Age extended terrain of the WSB with estimated depths unadjusted for the 3950 m of upward continuation associated with free-air gravity reduction. A closer evaluation of the free-air gravity power spectra response of the northern and southern WSB reveal an increase in crust and lithospheric thickness extending toward the southern interior of the basin, while concurrently highlighting the limitations of the methodology in estimating ice thickness due to inherent noise in shorter spectral wavelengths. Free-air gravity power spectra also proved useful in vertical constraint of subsequent isostatic anomaly modeling and inverse gravity solutions.

3.3. Isostatic Residual Anomaly Estimation

The isostatic gravity anomaly maps out departures of the measured gravity field from that generated by topography supported by variations in the thickness of the crust. As such, this method may highlight variations in the density of the crust, a key indicator for sedimentary basins. To further reduce the

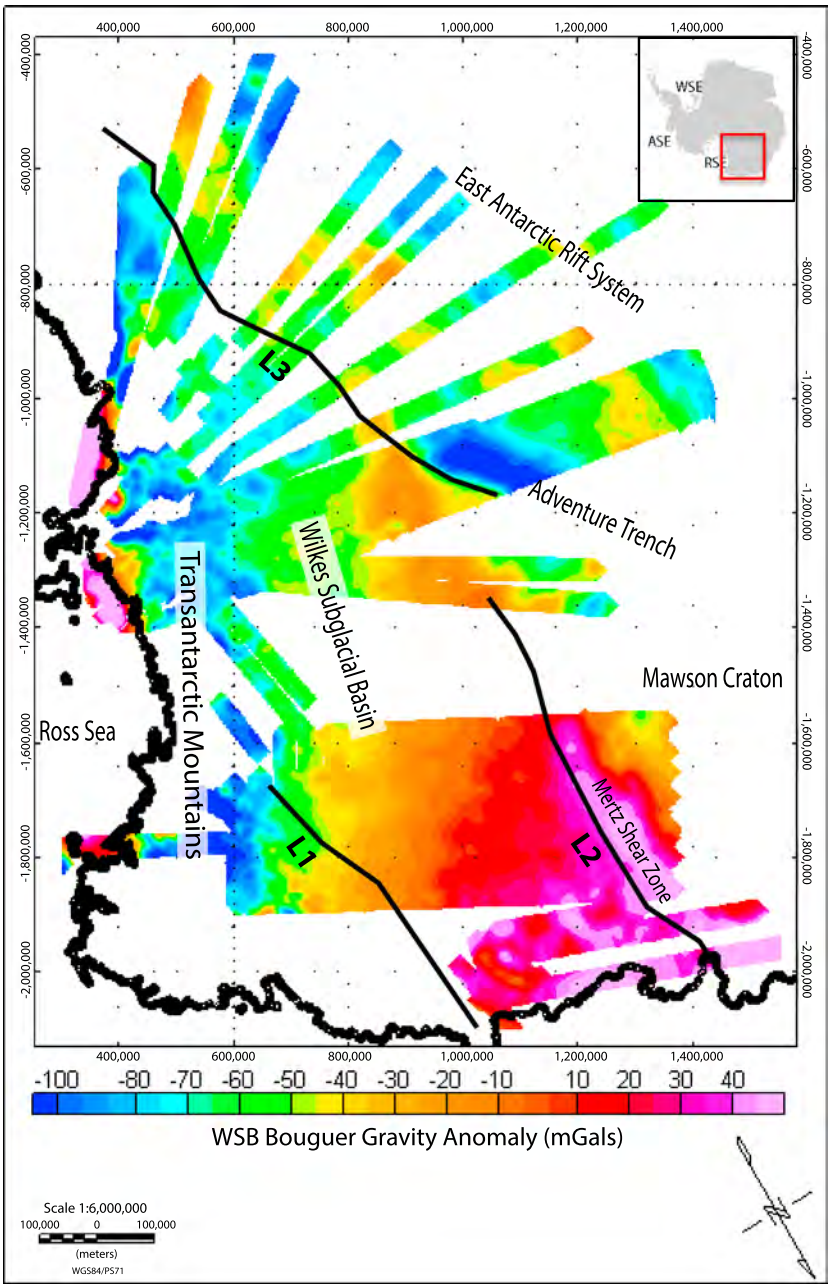

Figure 4. Wilkes Subglacial Basin Bouguer Gravity (mGal) anomaly ICECAP/IceBridge, WLK, and WISE-ISODYN data sets leveled to 3950 m. Bouguer anomaly depicts characteristically thinner lithosphere (red) in the extended basin interior (red) versus the characteristically thicker crustal root below the TAM (blue). Interpreted magnetic lineaments are also shown (L1–L3) indicating potential structural constraints to basin evolution.

gravitational anomaly, the isostatic impact of crustal thickness and associated Moho gravity effect had to be modeled and removed. Recent aerogeophysical investigations over the WSB, including the WLK survey to the south and the WISE-ISODYN in the north, were designed specifically as gridded surveys of near-constant altitude to more accurately assess the crustal structure below the WSB, Resolution Highlands, Adventure Trench, and adjacent TAM. Associated research including that of *Studinger et al.* [2004], *Ferraccioli et al.* [2009], and *Jordan et al.* [2013] have suggested structural control as opposed to the historic *Stern and ten Brink* [1989] hypothesis of flexure to explain the TAM and WSB topography.

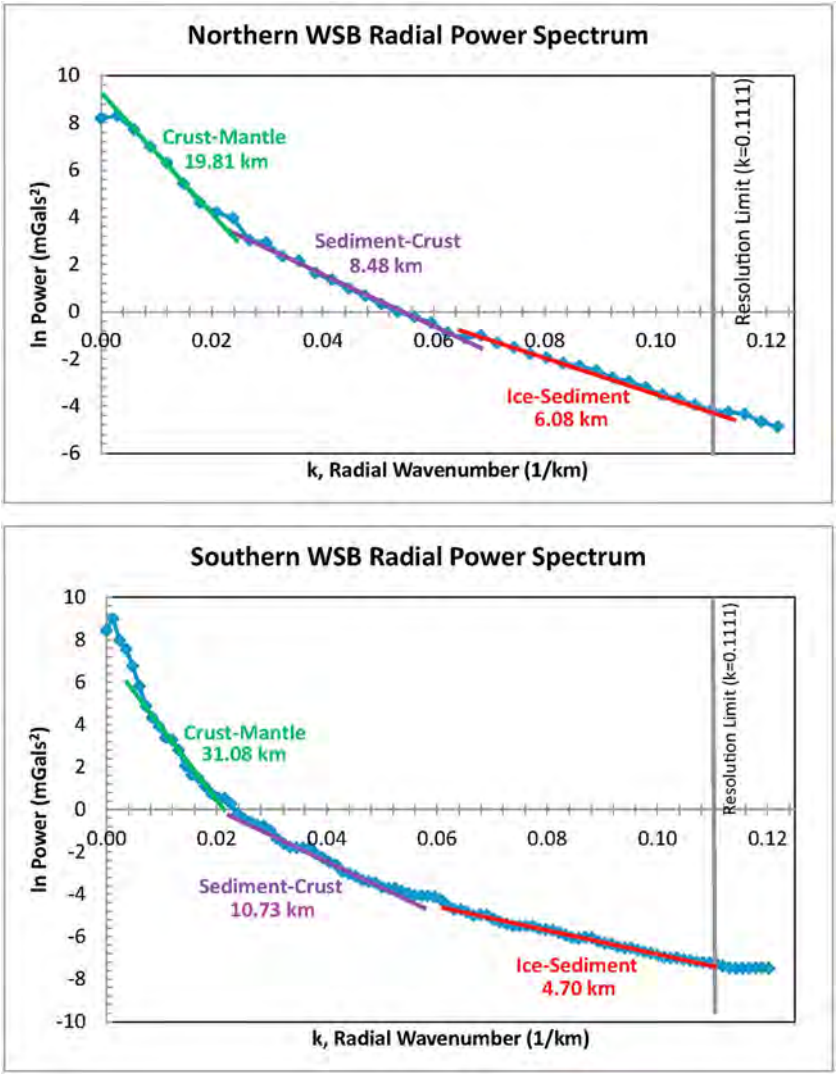

Figure 5. Wilkes Subglacial Basin free-air gravity radial power spectrum depth estimates average of slope energy spectrum showing density boundaries giving rise to distinct gravitational wavelength source depths—ice-sediment (red), sediment-crust (purple), and crust-mantle (green). Note the increasing Moho depth toward the WSB interior.

To assess hypotheses of prior research, two isostatic end-members (Airy isostasy and flexural) were initially generated to assess modeled crustal structure with elastic thicknesses of 0 and 90 km, respectively. Ultimately, consistent with the findings of *Studinger et al*. [2004], *Ferraccioli et al*. [2009], and *Jordan et al*. [2013], a locally compensated forward isostatic model with no inherent lateral strength [*Watts*, 2001] was confirmed to model 3-D variability of crustal thickness and the associated gravitational trend across the WSB with greater accuracy. Hence, an Airy isostatic 3-D regional structural digital elevation model [*Jachens and Griscom*, 1985] of the Moho surface was combined with ICECAP/IceBridge, WISE-ISODYN, and WLK airborne survey data and assigned ice, crust, and mantle densities of 0.92, 2.8, and 3.3 g/cm^3, respectively, to calculate the isostatic residual gravity anomaly using Geosoft's Oasis montaj® software (Figure 6). Lastly, GOCE satellite gravity data (downward continued to constant elevation of 3950 m) were utilized to remove regional, mantle-derived long wavelength data from the isostatic residual anomaly to yield a more accurate gravitational illustration of near-surface crustal density variations.

3.4. Total Magnetic Anomaly Interpretation

Regional magnetic anomaly data were compiled for the entire WSB including ICECAP/IceBridge, and the historical WISE-ISODYN and WLK surveys as detailed in *Ferraccioli et al*. [2009] and *Studinger et al*. [2004],

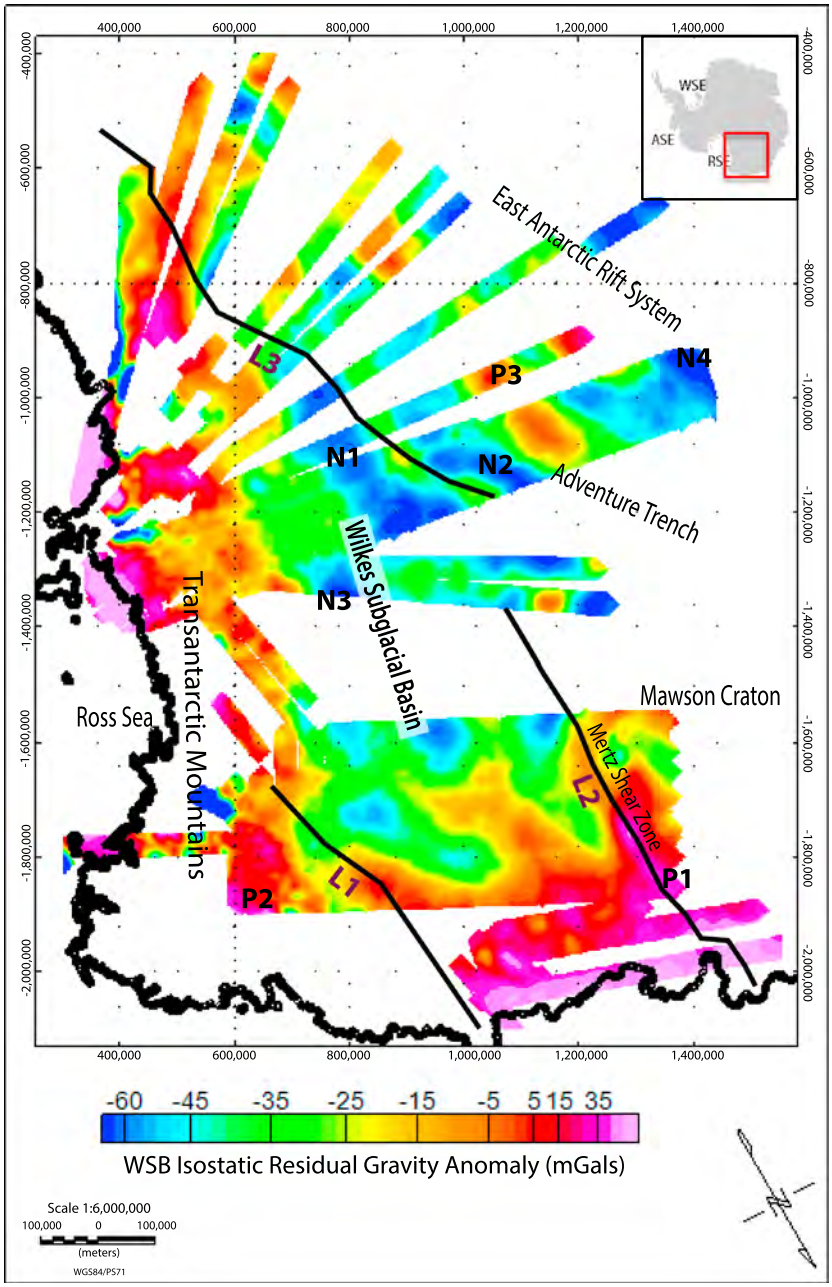

Figure 6. Wilkes Subglacial Basin residual airy isostatic corrected gravity (mGal) anomaly ICECAP/IceBridge, WLK, and WISE-ISODYN data sets leveled to 3950 m. Isostatic residual gravity anomaly results indicate gravitational deficiencies in the interior WSB relative to a simplified regional lithospheric structure model. P1, P2, and P3 mark positive Airy isostatic anomalies and reveal areas of near-surface high-density bodies, uplifted dense lower crustal rocks, and/or Moho uplift. N1 and N2 identify areas of negative Airy isostatic anomalies and reveal areas of potential near-surface low-density bodies including potential sedimentary basins. Interpreted magnetic lineaments are also shown (L1–L3) indicating potential structural constraints to basin evolution.

respectively. Major magnetic anomalies and lineaments were identified and labeled consistent with nomenclature established by *Ferraccioli et al.* [2009]. Although the extensional tectonic controls concerning the origins of the WSB have long been debated with hypotheses of lithospheric flexure, crustal thinning, and structural controls [*ten Brink and Stern*, 1992; *Ferraccioli et al.*, 2001, 2009], aeromagnetic features were identified and summarized here for the entire WSB to allow for lateral, basin-wide constraint along structural boundaries during subsequent subglacial sedimentary basin modeling.

Table 2. Wilkes Subglacial Basin Magnetic Depth to Basement Calculation Specifications

	Window Sizes (km)	Window Shift (km)	Depth: Minimum/Maximum (km)
Short wavelength	1, 3, 5	0.5	0.5, 5
Medium wavelength	5, 10, 15	2.5	2, 15
Long wavelength	10, 20, 30	5	5, 30

Beginning along the northern George V coastline, notable features include magnetic highs (MH7 and MH8) first identified by *Damaske et al*. [2003]. Based upon limited outcrops and the prior work of *Roland* [1991] and *Damaske et al*. [2003] suggested that the MH7 anomaly may be related to either (a) significantly thick portions of dolerite sill, (b) ice-covered Jurassic Kirkpatrick Basalts, or (c) thicker Jurassic mafic feeder bodies. With a more concentrated aeromagnetic grid, *Damaske et al*. [2003] described the WNW-ESE trending MH8 magnetic anomaly as notably more enigmatic with no direct correlation to outcrop. The same N-S trending magnetic anomaly high (MH4) that *Ferraccioli et al*. [2009] showed to extend across the western boundary of the WISE-ISODYN survey is shown here (Figure 3) to define the western edge of the WSB across some 1900 km. We interpreted this feature, flanked by a prominent magnetic lineament (L2), to define the extension of the Mertz Shear Zone (MSZ) Fault system extending from the George V coastline to the South Pole region. Based upon regional geologic conjugate margin hypotheses advanced by *Aitken et al*. [2014], *Boger* [2011], and *White et al*. [2013], the MSZ delineates the eastern extent of the Late Archean Mawson Craton underlying much of the EAIS from the WSB defined by Cenozoic extension and reworked passive margin sedimentation.

Another magnetic anomaly high, trending NW-SE across the eastern margin of the WSB and flanked by magnetic lineament L1 was first identified by *Damaske et al*. [2003] and then *Ferraccioli et al*. [2009] to be associated with Ross Age magmatic arc intrusions associated with the Prince Albert Fault System and the formation of the Prince Albert Mountains to the south. High-frequency magnetic anomaly highs associated with MH2 were observed coincident with broad mesa subglacial topography and were interpreted to be characteristic of Becon Supergroup lithologies massively intruded by Jurassic age Ferrar tholeiites [*Ferraccioli et al*., 2009].

With only adjacent TAM alpine rock outcrops, and no geologic exposures in the southern WSB, geologic constraint of associated magnetic anomaly data exceedingly speculative and sparse in historical literature. Lateral changes in magnetic anomaly texture, representing different wavelength content, can be distinguished across the region, however. Of particular note is the broad change in magnetic anomaly character across the southern WSB from east to west. From the TAM extending west into the WSB interior (MH9), the magnetic response is characterized by a broad magnetic anomaly high with short to long wavelength positive anomalies ranging from 5–10 km (±50 nT) to 100 km (100–250 nT) as detailed by *Studinger et al*. [2004]. Longer wavelength magnetic anomalies are generally interpreted to represent deep crustal response (>10 km depth) with shorter amplitudes characterizing shallower source depths of 1–10 km. The change in magnetic anomaly character from east to west approaching the MSZ (from MH9 to ML5 to MH5) is notable for the dramatic increase in amplitude and wavelength indicative of the transition from extended sediment-draped crust in the WSB to the thick, Late Archean Mawson Craton.

3.5. Depth to Magnetic Basement

The same principle applied in the spectral analysis of the gravity data referred to above can also be applied to magnetics data to assess the depth to magnetic (presumably crystalline) basement. Biased sampling inherent in the ICECAP/IceBridge variable flight line spacing precluded a full 3-D depth to basement (DTB) deconvolution due to variable wavelength information. However, by exploiting the high data density generated from consistent 10 Hz sampling rate along flight transects, magnetic DTB estimates could be derived via Werner 2-D deconvolution methods for short, medium, and long wavelengths [*Ku and Sharp*, 1983]. The 2-D Werner deconvolution method employed here utilized a moving window of specific width and distance at three different wavelength/window sizes (Table 2) such that the depth estimate returned directly corresponds to the window size to capture the full suite of depths characterizing the WSB.

DTB solutions exceeding the window width, or shallower than the sample interval are not likely to be valid; hence, source depths less than 50% of the narrowest window or more than 50% of the largest window width were discarded. To reduce noise in the short wavelength spectrum, a noise limit was implemented to reject

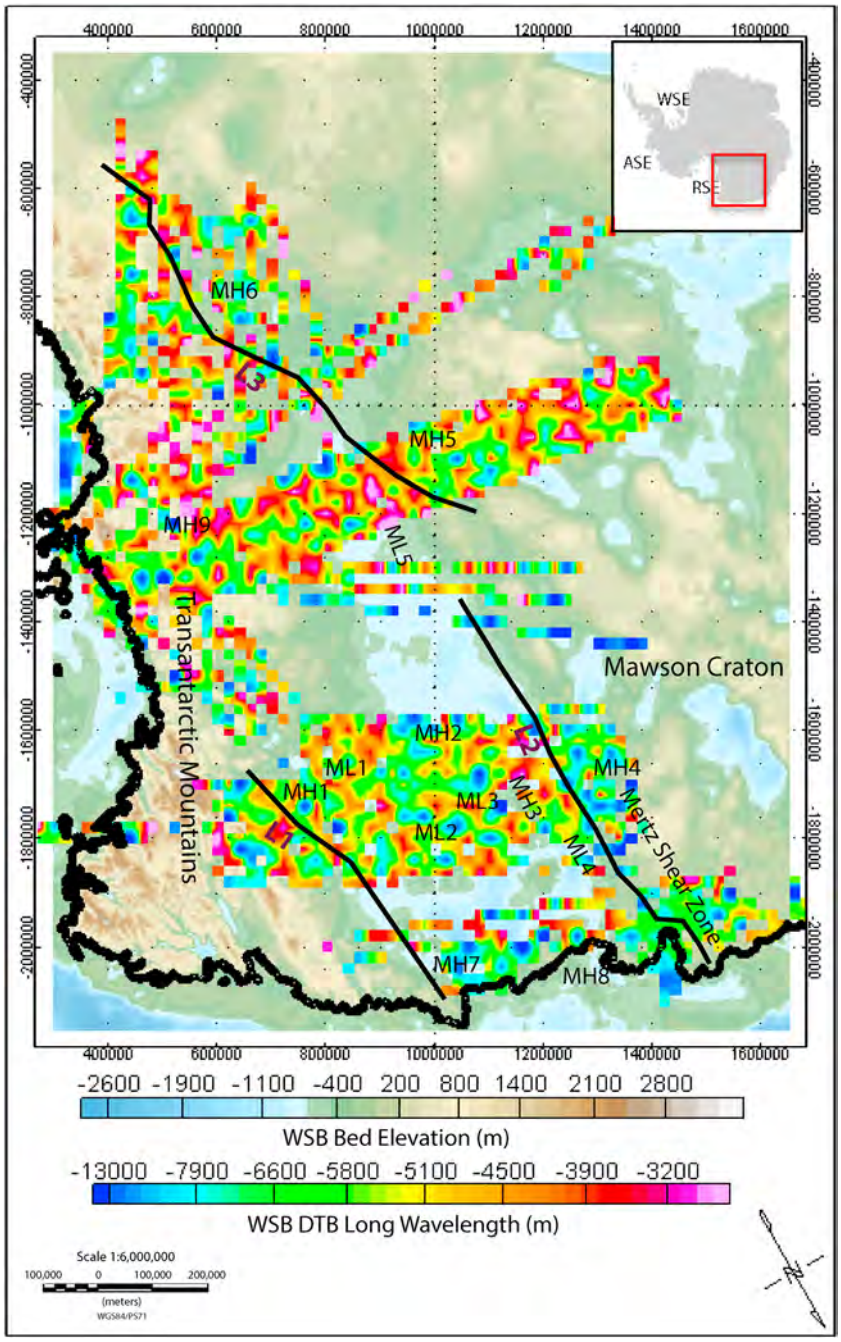

Figure 7. Wilkes Subglacial Basin Magnetic depth to basement (DTB) estimates via Werner 2-D deconvolution with mean direct gridding at 20 km. Long wavelength DTB results illustrate subice depth to magnetic basement provide vertical constraint for subsequent gravity inversion modeling. Bedmap2 bed elevations displayed as background [*Fretwell et al.*, 2013]. Interpreted magnetic lineaments are also shown (L1–L3) indicating potential structural constraints to basin evolution [*Ferraccioli et al.*, 2009; *Jordan et al.*, 2013].

analyses if the RMS anomaly amplitude did not exceed 20 nT. While DTB errors are difficult to quantify, calculated source depth estimates may vary on the order of 20–40% [*Kilty*, 1983].

DTB contact and dike solutions for all wavelengths were assessed against Geosoft's GM-SYS® gravity modeling solutions for comparison and vertical constraint. Long DTB wavelength solutions, found to most accurately constrain inverse gravity solutions illustrating the sedimentary basin-crystalline basement contact (Figure 9), are displayed with mean solutions direct gridded at 20 km in Figure 7.

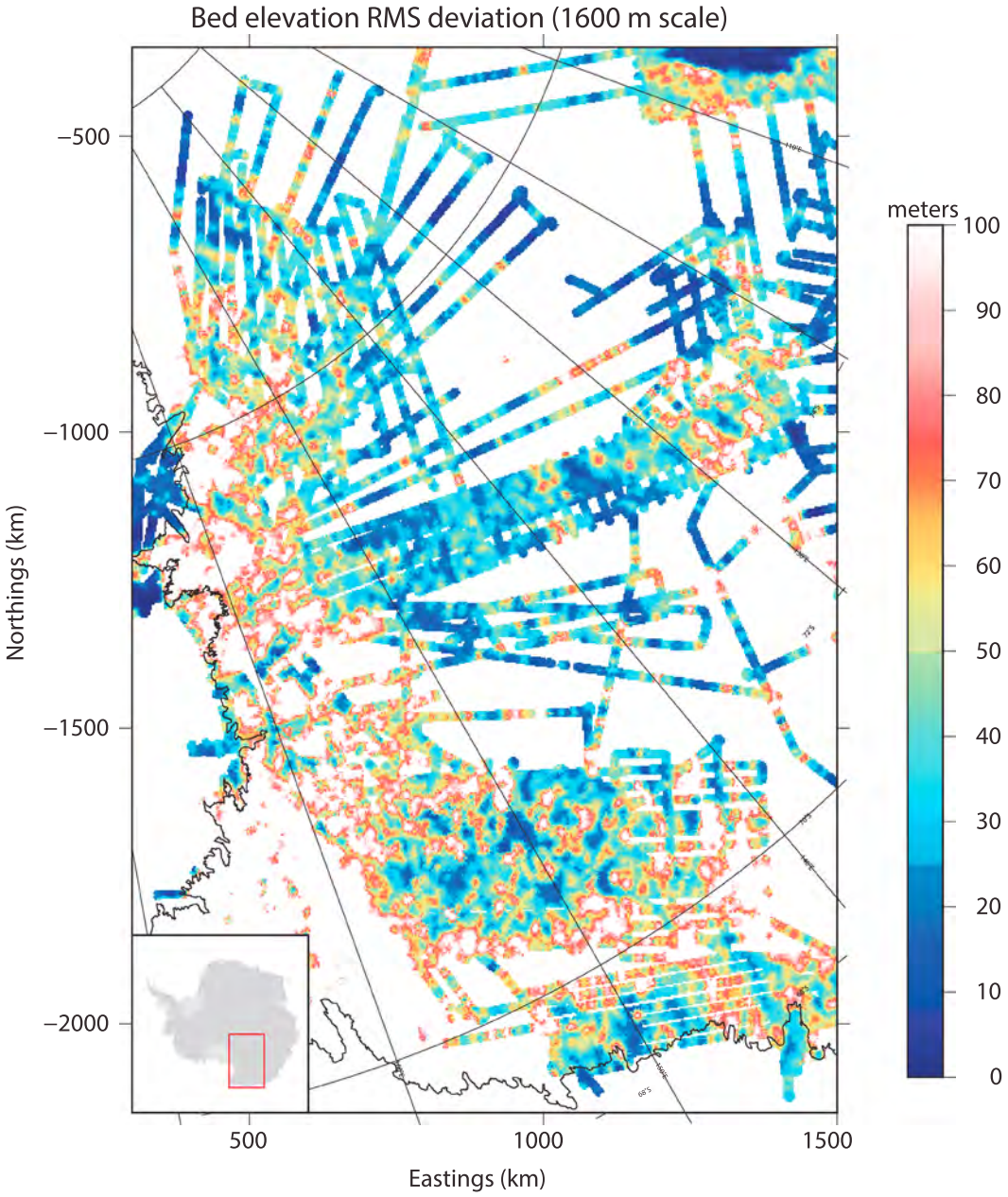

Figure 8. Wilkes Subglacial Basin radar roughness sediment mask—1600 m length scale illustrating smoother subglacial topography in blue and rougher in red/white.

3.6. Basal Roughness

Subglacial topographic roughness can be defined as the variability in vertical relief over a horizontal distance. Quantification of topographic roughness has been historically estimated as a relative measure of bed obstacle amplitude [*Shepard et al*., 2001] over horizontal scales of millimeters to hundreds of meters. More recent geophysical research quantifying subglacial bed roughness has focused on roughness scales of hundreds to tens of thousands of meters using a fast Fourier transform (FFT) technique over a range of wavelengths [*Taylor et al*., 2004]. The primary constraint of the FFT technique is the requirement that the along-track data must be continuous. Since sampling frequency data gaps are common in airborne geophysics, and our roughness were being utilized to help horizontally constrain gravity inversion results on the hundreds of meters scale, we opted against introducing interpolated data and strictly used the 60 MHz and 150 MHz

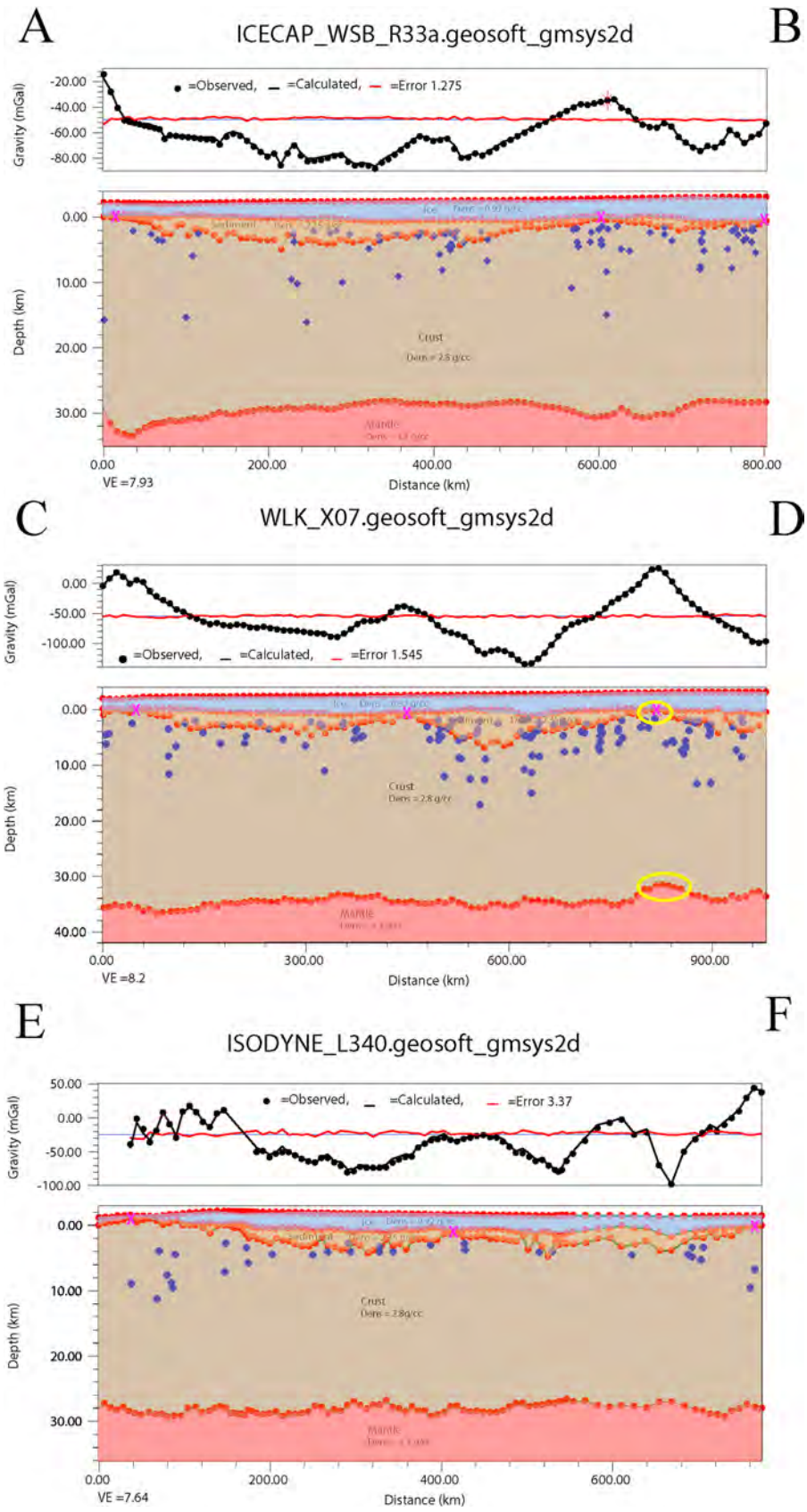

Figure 9

coherent ice-penetrating radar data from the combined aerogeophysical surveys. By assessing RMS deviation (v) results defined as the RMS difference in height separated by a step (Δx) and given by

$$v(\Delta x) = \left\{1/n \sum \left[(z(x_i) - z(x_i + \Delta x)\right]^2\right\}^{1/2} \quad (2)$$

where n is the number of sample points, $z(x_i)$ is the height of the surface at point x_i [*Shepard et al*., 2001; *Young et al*., 2011]. Roughness of the subglacial bed topography was estimated by assessing RMS deviation over a discrete length of 1600 m for which the heights of a rough surface are correlated with each other (Figure 8). Smooth regions appear blue, while rough, topographic highs appear white or red.

3.7. Sedimentary Basin Thickness Modeling

The variable distance between radial flight line patterns resulted in wavelength bias when attempting traditional 3-D steepest descent gravity inversion techniques to estimate subglacial sedimentary basin thicknesses, so 2-D free-air gravity inversion algorithms were exploited using Geosoft's GM-SYS® modeling package [*Talwani and Ewing*, 1960]. Model density values, ice (0.92 g/cm^3), sediment (2.35 g/cm^3), crust (2.8 g/cm^3), and mantle (3.3 g/cm^3), were constrained with prior seismic and gravity research in the WSB region [*Ferraccioli et al*., 2001] and assessed versus theoretical estimates [*Bahr et al*., 2001]. Topographic surfaces for ice, bed, and manually smoothed Airy Moho surfaces were held fixed with iterative inverse solutions performed on the model until the error between the calculated and measured gravitational response was approximately 3 mGal or less. The resultant 2-D subglacial sedimentary basin isopach estimates were calculated along track, interpolated, and gridded using a minimum curvature method with a cell size of 2 km (Figure 9).

Airborne magnetic anomaly data, often indicative of changes in crustal structure or overburden, were utilized for lateral constraint of subglacial sedimentary basin locations and long wavelength DTB data for vertical constraint of the sediment to crystalline bedrock transition. In the northern WSB, the Eastern Basin is constrained by a distinct magnetic lineament associated with Ross Age magmatic arc intrusions (L1 in Figure 3) and aligned with the Prince Albert Fault System [*Ferraccioli and Bozzo*, 1999]. By contrast, the Western Basin in the northern WSB is confined by magnetic lineament L2 (and a strong positive Airy isostatic gravity anomaly) representing a major fault aligned with the MSZ and suggesting that inherited tectonic structures greatly influenced later basin formation [*Ferraccioli et al*., 2009; *Jordan et al*., 2013]. In the southern WSB, magnetic lineament L2 continues to define the western boundary of the subglacial sedimentary basin and the unreworked Proterozoic assemblages of the Mawson Craton [*Ménot et al*., 2007] extending between ML5 and MH5 toward the South Pole.

Additional crust and lithospheric anomalies in the WSB include localized positive gravity anomalies in both 3-D Bouguer and Airy isostatic gravity responses. First noted by *Studinger et al*. [2004] in the southern WSB following the WLK aerogeophysical survey, these positive observed gravity anomalies such as P3 in Figure 6 require a near-surface high-density body or a Moho uplift to generate a similar positive Airy model response (e.g., Profile C-D in Figure 9). *Jordan et al*. [2013] described similar positive gravity responses (e.g., P1 and P2) in the northern WSB (Figure 6), attributing these anomalies to either dense exposed metasedimentary rocks or uplifted dense lower crustal rocks, noting similar features in the Mesozoic Arc terranes of the Antarctic Peninsula [*Ferraccioli et al*., 2006].

Moho depths initially derived from simple Airy isostatic calculations were manually smoothed, and basin isopachs iteratively adjusted until modeled gravity results reflected observed. Because 2-D inverse gravity modeling is nonunique, the initial layered density models were kept as simple as possible with resultant isopachs along each 2-D flight line compiled and subsequently interpolated using a minimum curvature technique with 2 km grid spacing (Figure 10).

Figure 9. Wilkes Subglacial Basin 2-D GM-SYS® forward gravity model profiles with magnetic DTB results (see Figure 10 for map profile transects)—red dots represent model horizons with densities posted. Black dots represent observed free-air gravity with modeled gravity depicted as a black line. Error across the 2-D model depicted as a red line. Blue circles represent long wavelength magnetic DTB contact and dike results. Yellow ellipses identify areas of potential Moho uplift or near-surface high-density lower crustal rocks. Purple crosses indicate RMS roughness pinning points for lateral constraint of inverse gravity solutions.

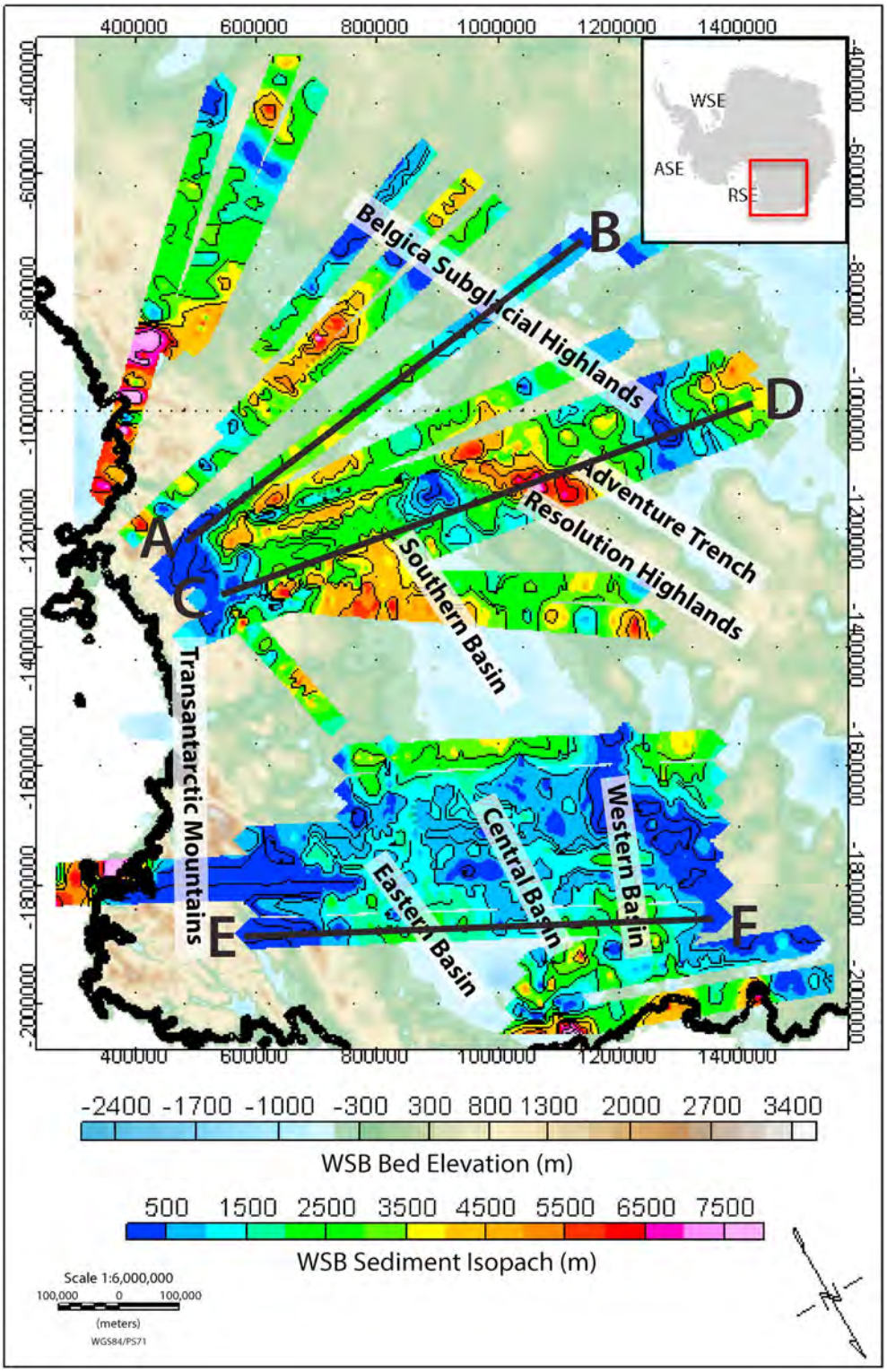

Figure 10. Wilkes Subglacial Basin sediment isopach (meters) with subbasins identified: 2-D GM-SYS® gravity model transects also shown (Figure 9). Bedmap2 bed elevations displayed as background [*Fretwell et al.*, 2013].

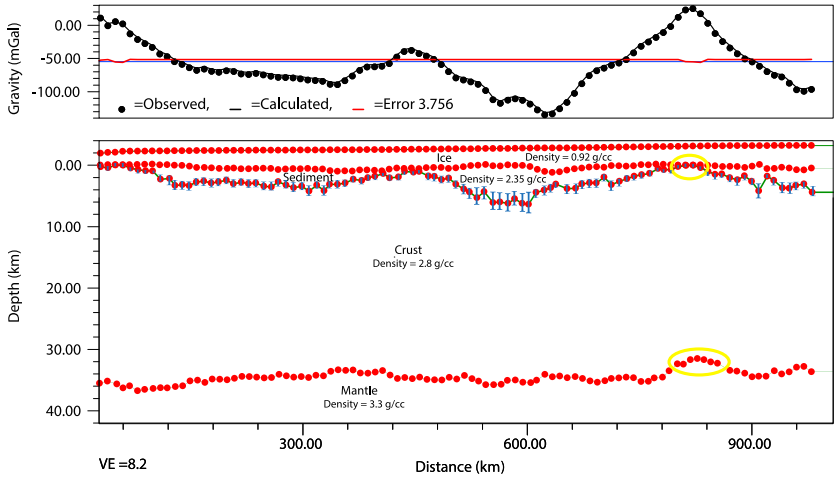

Figure 11. Results of inversion of gravity data along profile C-D (Figure 10) of the Wilkes Subglacial Basin. Observed and computed anomaly and corresponding model with variance represented as vertical bars. Yellow ellipses identify areas of potential Moho uplift or near-surface high-density lower crustal rocks.

While a significant variation in modeled sediment densities was discovered in published literature for Wilkes Land, prompting an evaluation of sediment densities from 1.85 g/cm^3 [*Filina et al.*, 2008] to 2.4 g/cm^3 [*Ferraccioli et al.*, 2001], empirical examination of probable sediment densities at these burial depths with an average of 2 km of overlying ice at effective pressures on the order of 70–90 MPa and estimated sediment porosities of 15–18%, resulted in subglacial sediment density estimates of 2.3–2.4 g/cm^3[*Gueguen and Palciauskas*, 1994; *Bahr et al.*, 2001; *Zoback*, 2010]. Based on these empirical estimates and prior modeled WSB sediment densities [*Ferraccioli et al.*, 2001; *Studinger et al.*, 2004], final gravity models were constructed using a subglacial sediment density estimate of 2.35 g/cm^{3}resulting in average sedimentary basin thicknesses for the northern and southern WSB of 1144 m ± 179 m and 1623 m ± 254 m, respectively. Gravity modeling across more finite subbasins, including the east (~2 km), central (~3 km), and western (~4 km) basins in the northern WSB [*Ferraccioli et al.*, 2009], the southern WSB (~5 km), and the Adventure Subglacial Trench (>6.5 km) contained substantially thicker sediment thicknesses as detailed in Figure 10. Analogous to the findings of *Studinger et al.* [2004], the Adventure Subglacial Trench sedimentary deposits do not entirely fill the trench itself, but form much of the eastern shoulder shoaling to the west and the shallow DTB response characteristic of the Belgica Subglacial Highlands.

3.8. Uncertainty Estimation

While depth to magnetic basement and radar roughness estimates can be utilized to constrain vertical and horizontal subglacial sediment distribution models, respectively, inversion of gravity anomalies is inherently a nonunique solution with sizeable trade-offs between density and geometry. Using a nonlinear approach to solving the inverse problem, density contrasts were established between geologic interfaces and the inversion constrained with depths at isolated points along the interface [*Leao et al.*, 1996]. Despite this, gravity inversion equations remain ill posed, such that instead of presenting a finite solution uncertainty estimates were quantified to assess the validity of the inverse problem.

East-west flight profiles were inverted using the Parker-Oldenberg gravity inversion algorithms included as part of Geosoft's Oasis montaj® software suite vertically constrained with radar ice thickness data and laser-derived topography. Initial results with no basal depth range constraints provided good agreement between the computed and observed gravity anomalies with error reduced to 0.04 in Figure 11 profile example resulting in an average sediment thickness of 2209 m ± 180 m with uncertainties based upon variability in estimated subglacial sediment densities. It should be noted that despite vertical sediment thickness uncertainties, the lateral sediment distribution pattern remains consistent. While the variability of the depth values was initially large, depicted by the blue vertical lines in Figure 11, these uncertainties were subsequently minimized by constraining the minimum and maximum depths of the bedrock surface using vertical magnetic DTB limits to the upper and lower bounds of sediment thickness. Several statistical measures of

uncertainty, including mean, variance, and standard deviation, were calculated herein based upon the multitude of inverse models generated. Consistent with the findings of *Roy et al*. [2005], we found the uncertainty estimates of density models inverted from gravity data do not accentuate the limitations of the inversion process, but actually strengthen the reliability of the results.

4. Discussion and Interpretation

4.1. Crustal Structure From Free-Air and Bouguer Gravity

WSB airborne free-air gravity results (Figure 2) mimicked bed topography as would be expected with free-air gravity lows corresponding to topographic bed elevation lows in the basin and free-air gravity highs corresponding to topographic bed elevation highs. Of particular note are the three northern WSB basins, east, central, and western, that *Ferraccioli et al*. [2009] identified with regional free-air anomalies on the order of ~ −60 mGal and a central, interior southern WSB gravity low exceeding ~150 mGal. The Transantarctic Mountains are characterized by strong positive free-air anomalies averaging 50–60 mGal, with local negative anomalies < -100 mGal typify the Cook and Byrd glacial valleys.

By removing the free-air topographic bias in the gravity data and further isolating the geologic signal, the Bouguer gravity results (Figure 4) reflect crustal thickness variability and the isostatic load of topographic variations and increasing ice load toward craton interior. Thinner continental crust associated with the rifted, passive, continental margins is particularly apparent as a positive Bouguer anomaly at the Southern Ocean and Ross Sea boundaries. Within the northern WSB a general east to west increasing trend in Bouguer anomalies is noted from ~ −100 mGal to 100 mGal. The western boundary of the northern WSB is demarcated by the MSZ and the associated positive Bouguer response thereby extends some 900 km to the south as noted by *Jordan et al*. [2013]. Bouguer anomalies decline substantially to ~ −70 mGal in the central southern WSB subbasin and to <-200 mGal in the Adventure Subglacial Trench. The fringes of a deep interior basin termed the East Antarctic Rift system (EARS) by *Ferraccioli et al*. [2011] can also be distinguished toward the end of the ICECAP/IceBridge radial flight lines with a distinct negative Bouguer response of ~$<$100 mGal. The EARS, Adventure Trench, and southern WSB are all characterized by low bed roughness (Figure 8) indicative of smooth sedimentary basal ice conditions. In contrast, the faulted, extensional relief of the northern WSB crust and associated tectonic history with only a thin sediment drape is revealed as elevated bed roughness and coarser subglacial basal ice conditions for all but the Cook and Mertz glacial catchments and the east, central, and western subbasins identified and described by *Ferraccioli et al*. [2009] and *Jordan et al*. [2013].

To assess the probability of a midcrust discontinuity, gravity power spectra was plotted against wave number (Figure 5) revealing a subtle change in slope at a lithospheric depth associated with the Crust-Moho boundary, and an additional change in slope associated with a subglacial sedimentary basin density contrast in the shallow crust. Based on the resultant least squares line segment slopes, the best fit Moho depths for the WSB, unadjusted for the 3950 m of free-air gravity upward continuation, fell between 20 and 31 km with no apparent midcrust discontinuity as would be expected from the Proterozoic EAIS lithospheric craton. Crust spectral response indicated increasing lithospheric thickness toward the southern interior of the WSB, with the base of sediment increasing from an unadjusted depth of 8.48 to 10.73 km (4.53 to 6.78 km adjusted), and the Moho depth increasing from an unadjusted depth of 19.81 to 31.08 km (15.86 to 27.13 km adjusted). More finite lateral spatial changes in lithospheric boundaries were not performed across the WSB using spectral analysis techniques as a result of the variable wavelengths inherent in the airborne gravity data due to the radial flight pattern design. Regional body wave tomography analyses confirm our spectral analysis results here with recorded Moho depths on the order of 25–35 km for the WSB [*Baranov and Morelli*, 2013; *Lloyd et al*., 2013] and no midcrustal density contrast. While *Bannister et al*. [2003] found midcrustal discontinuities in the Transantarctic Mountains at approximately 8–14 km depth, the associated seismic velocity boundary did not extend west into the WSB and East Antarctic craton.

4.2. Geological Context From Isostatic Anomalies and Magnetic Anomalies

Because expansive ice loads often result in a direct isostatic response [*Watts*, 2001], lithospheric flexure associated with WSB basal topography and ice loads was estimated using a locally compensated Airy forward isostatic model for the Moho boundary and generalized constraints from the gravity power spectra analysis (Figure 5). The resultant isostatic residual gravity deficiencies <-150 mGal, in the southern WSB interior and the subglacial Adventure Trench are reflective of near-surface crustal mass deficiencies in the model. Given

the lack of recent volcanism and characteristically low mantle-derived geothermal flux for the East Antarctic craton in the Wilkes Land region [*Pollard et al*., 2005], the negative isostatic anomalies over the relatively cool crust could most likely be attributed to low-density bodies of a range of compositions [*Aitken et al*., 2014; *Damiani et al*., 2014]. Significant low isostatic residual gravity anomalies also appear near the ends of several ICECAP/IceBridge flight lines across the southern WSB, potentially associated with a sizeable subglacial sedimentary basin in the EARS region.

The isostatic residual anomaly map (Figure 6) reveals several distinct positive (P1-P3) and negative (N1-N4) anomalies. Notable anomaly trends are readily apparent in the data, including the N-S trend of anomalies P1, P2, and N3, and the NW-SE trends of P3, N1, N2, and N4. Based upon these anomalies, previous authors have suggested single coupled flexural systems [*Studinger et al*., 2004] and inherited tectonic structure controls [*Ferraccioli et al*., 2009; *Jordan et al*., 2013] to explain the structure and origin of the WSB. The addition of the more expansive ICECAP/IceBridge airborne gravity data, specifically across the southern WSB, indicate a greater diversity of tectonic structure between the northern and southern WSB potentially dictating geomorphologic development and basin evolution since the Cambrian [*Aitken et al*., 2016].

Positive gravity anomaly P1 can be traced from the Terre Adelie coast to over 900 km inland and is aligned N-S with magnetic lineament L2 [*Ferraccioli et al*., 2009] and the MSZ. *Jordan et al*. [2013] interpreted this boundary to represent the margin of the Proterozoic assemblages of the Mawson Craton contrasted with Ross Age back-arc basin assemblages. The MSZ is undoubtedly the most extensive, significant structural boundary in the region that establishes the western boundary of the Ross Orogen magmatic activity [*Gibson et al*., 2013] while defining the western extent of the WSB separating the Mawson Craton from the reworked passive margin sediments in the WSB interior [*White et al*., 2013]. The interpreted conjugate to the MSZ across the Southern Ocean is the Coorong Shear Zone in the Gawler Craton of Southern Australia [*Gibson et al*., 2013]. Additional identified northern WSB faults and magnetic lineaments, most likely emerging as reactivated Ross Age fractures during Cretaceous extensional tectonics associated with the West Antarctic Rift [*Jordan et al*., 2013], correlate well with existing subbasin structures in the WSB including the eastern, western, and central basins identified by *Ferraccioli et al*. [2009].

Farther to the east in the northern WSB, positive isostatic anomaly P2 also indicates a N-S trend and has been interpreted to represent metasedimentary rock exposures of the central Wilson Terrane in a "pop-up" thrust structure [*Flottmann et al*., 1993; *Laufer et al*., 2006; *Jordan et al*., 2013]. By contrast, the NW-SE regional trend of the subglacial Adventure Trench, the EARS, and associated anomalies P3 and N1, N2, and N4 suggest disparate structural controls between the northern and southern WSB. Deep glacial valleys associated with the Cook and adjacent Mertz glaciers appear to have exploited N-S trending zones of crustal weakness during tectonic reactivation associated with the WAR plate extension in the northern WSB to cut across the basin bounding MSZ in the area of the western central basins originally identified by *Ferraccioli et al*. [2009].

The origin and nature of the Adventure Subglacial Trench region, characterized by strong negative Bouguer and isostatic residual anomalies immediately adjacent to strong dipole-patterned positive anomalies, has been particularly moot in recent literature with peak to trough amplitudes exceeding 120 mGal [*Ferraccioli et al*., 2001; *Studinger et al*., 2004; *Jordan et al*., 2013]. While the similar wavelength, amplitude, and trend of the positive-negative dipole in the southern WSB has been interpreted as a coupled compressional flexural system, analogous to the fold thrust belts of the Alps and Appalachians [*Studinger et al*., 2004], the geomorphologic evolution of the northern WSB appears distinctly different with N-S magnetic lineament and isostatic residual gravity anomaly trends characteristic of the exposed Ross orogenic systems in Northern Victoria Land [*Jordan et al*., 2013]. Hence, unlike the northern WSB, the tectonic signature for the southern WSB may extend beyond the Ross Orogen to the collision of the Mawson Craton with Indo-Antarctica and subsequent extensional forces associated with the Terra-Australis Orogeny prompting motion within the Mawson Craton along the NW-SE orientation of the transverse Aurora Fault [*Aitken et al*., 2016]. This hypothesis of WSB basin evolution influenced by at least two orogenies and TAM uplift may not only best account for the development of disparate trends in aerogeophysical signatures but also explain the potential for flexural downwarp during the accretionary orogenesis of the Terra-Australis Orogeny [*Aitken et al*., 2016] followed by subsequent Ross Orogen tectonics and back-arc basin development to the east [*Ferraccioli et al*., 2009]. This complex WSB tectonic history may also best illustrate the disparate inherited structural geometries and aerogeophysical trends caused by intraplate weaknesses from the north to south WSB.

4.3. Sediment Distribution From Depth to Magnetic Basement and Basal Roughness

Magnetic DTB results were segregated by wavelength based upon 2-D Werner deconvolution window size and plotted along profile against Geosoft's GM-SYS® gravity modeling results. Shorter spectral wavelength noise was appreciable such that solutions were clustered to reveal areas along the flight profile where DTB results remained less than −500 m. These and other anomalously shallow DTB estimates in well-sampled areas, occurring above the base of the ice sheet, were found to be within the error of basal ice elevations and thereby rejected prior to gridding. Sparsely sampled areas toward the WSB interior were not culled and therefore may have led to negative skewness and some erroneous minimum DTB values. However, all skewed minimum values fell within the inherent variability of DTB calculations estimated at 20–40% [*Kilty*, 1983].

Areas of anomalously shallow DTB results also generally correlated with inverse gravity models revealing little to no sediment (Figure 9) and were therefore interpreted to represent ice overlying crystalline basement rocks [*Aitken et al*., 2014]. Short and medium DTB wavelength solutions were scattered throughout the gravity-modeled subglacial sedimentary basin profiles reflective of remnant magnetism inherent to Beacon sandstone deposits with mafic sills [*Ferraccioli et al*., 2009] or Ferrar sills overlying Beacon sediment [*Studinger et al*., 2004]. Long magnetic DTB wavelengths (10–30 km), responding to deeper magnetic sources, proved most suitable in vertical constraint of the sedimentary basin-basement boundary given the primary magnetic anomaly amplitudes across the WSB. This final deconvolution window size range not only provided the best vertical constraint to gravity basin modeling but also proved consistent with previous aeromagnetic reduction findings for the northern WSB [*Ferraccioli et al*., 2009].

Subglacial bed surface roughness was quantified by evaluating RMS deviation over correlation length on scales of 1600 m. Results were subsequently gridded at 2 km, using a minimum curvature approach, and plotted (Figure 8) with GMT [*Wessel and Smith*, 1998]. These sediment mask results revealed significantly smoother surfaces across the interior of the southern WSB, Adventure Trench, EARS, and central and western basins of the northern WSB with RMS height deviations falling below 10 m over the respective length scales. RMS deviation over correlation length is impacted not only by changes in RMS deviation but also by larger correlation lengths associated with smoother and rougher surfaces by smaller lengths [*Shepard et al*., 2001]. As such, subglacial and subaerial highlands (including Dome C, the Resolution subglacial highlands, and the TAM) resulted in RMS height deviation values exceeding 70 m at the 1600 m correlation length scale. The distinct transition between rough and smooth bed surfaces at the subglacial basin edge in the interior WSB provided additional lateral constraint as pinning points during subsequent sedimentary basin modeling efforts (Figure 9). These smooth bed features remain consistent with the presence of weak, unconsolidated sediments across interior portions of the WSB [*Alley et al*., 1987].

4.4. Modeling and Interpretation of Sedimentary Basins

Prior to actively modeling potential sediment thicknesses across the WSB, a combination of constraints from DTB, basal roughness, and isostatic residual anomalies suggested that particularly the southern WSB may contain substantially more sediment than previously suggested by *Studinger et al*. [2004]. Subsequent 2-D forward gravity modeling (Figure 10) revealed that much of the interior WSB, in areas characterized by smooth bed surfaces in radar sediment mask analyses (Figure 8), exhibited a minimum of 1000 m of overlying subglacial sediment thickness. Three distinct subbasins, the central southern WSB, and the central and western basins in the northern WSB, that were characterized by RMS deviation versus correlation length estimates of less than 10 m at the 1600 m scale all contained sedimentary basin isopach results in excess of 3 km. The central southern WSB contained an average sediment isopach value of 1623 m ± 254 m with gravitational response across flight transects resulting in sediment thicknesses in excess of 6 km in certain locations (Figure 9). The northern WSB, by contrast, revealed lower average sediment isopach values of 1144 m ± 179 m. With gravitational models along flightlines crossing the eastern, central, and western basins of the northern WSB, illustrating maximum subglacial sediment thicknesses in excess of 2.5 km, 4 km, and 3.5 km, respectively. These isopachs can be compared to conjugate margin coastal plain and deltaic-marine sedimentation in the Otway Basin of South Australia containing some 5 km of post Late Cretaceous Sherbrook Group deposition [*Krassay et al*., 2004]. Estimated sediment volumes based on the calculated WSB isopachs with 15–18% porosity would be on the order of 128,094 ± 52,399 km^3 for the central southern WSB, and 7188 ± 2940 km^3, 30,596 ± 12,515 km^3, and 21,524 ± 8805 for the eastern, central, and western basins in the northern WSB, respectively. The predominance of thicker, more expansive subglacial sedimentary sequences in the southern WSB with

correspondingly thinner, more restricted subglacial sedimentary basins in the northern WSB is consistent with selective linear erosion along regional hydraulic and ice flow and erosion pathways and greater ice sheet stability in the interior southern WSB where basal elevations lie above present-day sea level [*Jamieson et al*., 2014].

In addition, more recent studies by *Schroeder et al*. [2013], conducted in the Thwaites Glacier catchment of West Antarctica, suggest that basal ice conditions in the interior portions of the WSB may be controlled by distributed/dendritic subglacial hydraulic networks in equilibrium with overlying ice that reduce basal drag versus the more channelized subglacial hydraulic canal networks characterizing the lower catchment regions. If plausible, increased basal drag and associated erosion and scouring would be more prevalent in the northern versus the southern WSB, further supporting a northern WSB characterized by thinner subglacial sedimentary deposits with significant accumulations only in restricted, channelized basins. With northern WSB bed elevations averaging an excess of 500 m below sea level, the susceptibility of this region to eustatic forcing including the likelihood of significant sediment deformation fueling basal EAIS dynamics in the region [*Alley and Blankenship*, 1987] can be substantiated. However, questions remain as to whether the concentration of significant subglacial sedimentary sequences to deeper channelized subglacial basins in the northern WSB and the connectivity of these basins to predominant outlet glacier catchments in the region, including the Cook, Ninnis, and Mertz Glacier catchments, would temper broader retreat of the ice sheet into the WSB interior. Recent WSB paleoclimate models and ice volume assessments by *Cook et al*. [2013], *Mengel and Levermann* [2014], and *Pollard et al*. [2015] support a more dynamic EAIS with broader WSB ice sheet instability along the George V Coast during the Pliocene than had been previously suggested.

Given that areas of smooth subglacial morphologies promote faster ice flow that in turn promote additional topographic smoothing [*Rippin et al*., 2011], and current sediment volume estimates do not account for widespread lowering of the East Antarctic landmass since the Eocene [*Wilson et al*., 2012], it is probable that a majority of sediment eroded from the continental interior has not been transported to the margins but is instead preserved in interior subglacial basins. Internal WSB sedimentary basin development has consistently been shown to be confined to rift basins [*Ferraccioli et al*., 2011; *Jordan et al*., 2013], areas of selective overdeepening [*Rose et al*., 2013], and subglacial lake development [*Jamieson et al*., 2014]. The dendritic character of the continental-scale subglacial hydraulic networks [*Wright et al*., 2012; *Jamieson et al*., 2014] support a hypothesis that basin-scale glacial erosion and ice flow is dictated by tectonic structure [*Jamieson et al*., 2005; *Jamieson and Sugden*, 2008] and that glacial erosion in the WSB continues to exploit inherited preglacial fluvial networks. The paleoclimatic signatures contained within these preserved subglacial sedimentary sequences may contain records of past fluvial and ice dynamics extending well beyond the Cenozoic given the complex tectonic evolution of the WSB. In particular, the broad subglacial sedimentary basins of the southern WSB may have the best potential to preserve a more extensive paleoclimatic record given the greater lateral extent of deposition versus the northern WSB sedimentary basins and a more distal position relative to the fold-and-thrust belt between the Mawson Craton and the Ross Orogen [*Ferraccioli et al*., 2009]. Nevertheless, additional seismic and/or aerogeophysical data over preliminary targets may be warranted prior to actively pursuing potential subglacial access drilling activities.

5. Conclusions

Here we have presented the first comprehensive subglacial sediment isopachs for the WSB region derived from airborne gravity measurements and corroborated against other geophysical data sets that are known sedimentary basin indicators. The central southern WSB contained an average sediment isopach value of 1623 m ± 254 m with sediment thicknesses in excess of 3.5 km in certain locations, while the northern WSB revealed average sediment isopach values of 1144 m ± 179 m and subglacial sediment thicknesses in excess of 2.5 km several subbasin locations. Estimated sediment volumes, presuming 15–18% porosity, appear to be on the order of 128,094 ± 52,399 km^3 and 59,308 ± 24,260 km^3 for the southern and northern WSB, respectively.

The substantial increase in subglacial sedimentary basin thickness and volume to the south supports a hypothesis of relative ice sheet stability across the WSB interior since the mid-Miocene [*Jamieson et al*., 2010] with more frequent Pliocene to Pleistocene ice sheet retreat/advance cycles impacting the northern WSB [*Miller et al*., 2012; *Cook et al*., 2013] across century to thousand year timescales [*Pollard et al*., 2015]. The presence of thicker subglacial sedimentary basins in the southern WSB, proximal to both TAM and EARS highlands, may be the result of a combination of deposition during preglacial to oscillatory temperate/polythermal glacial regimes during the early Miocene/late Oligocene as suggested by *Krassay et al*. [2004] for the conjugate Australian margin and

Young et al. [2011] for the adjacent Aurora Subglacial Basin (ASB), respectively, with subsequent basin preservation beneath a more permanent, stable polar ice sheet during the Pliocene-Pleistocene. To be certain, quantification of the extent, thickness, and character of the WSB subglacial strata has broad implications for EAIS boundary conditions used in global climate and eustatic models and may also identify some of the best preserved paleoclimatic data associated with EAIS development and dynamics over this region and thus be a future target for subglacial access drilling once the technology matures.

Acknowledgments

This work was supported by National Science Foundation (NSF) grant ANT-1143836; NASA grants NNX09AR52G, NNG10HP06C, and NNX11AD33G; NERC grant NE/D003733/1; the Jackson School of Geosciences; and the G. Unger Vetlesen Foundation. This paper is in part a result of the ICECAP collaboration between the USA, UK, and Australia to Investigate the Cryospheric Evolution of the Central Antarctic Plate through airborne geophysical surveys, and a compilation of historical data collected by the British Antarctic Survey (BAS) and NSF's Support Office for Aerogeophysical Research (SOAR) under NSF grants OPP-9120464, 9319369, and 9319379. Logistical support was provided by the U.S. Antarctic Program, the French Polar Institute, the Italian Antarctic Programme (PNRA), and the Australian Antarctic Division. Many thanks to two anonymous reviewers for their helpful and constructive commentary. This is UTIG contribution 2833.

References

Aitken, A. R. A., D. A. Young, F. Ferraccioli, P. G. Betts, J. S. Greenbaum, T. G. Richter, J. L. Roberts, D. D. Blankenship, and M. J. Siegert (2014), The subglacial geology of Wilkes Land, East Antarctica, *Geophys. Res. Lett.*, *41*, 2390–2400, doi:10.1002/2014GL059405.

Aitken, A. R. A., P. G. Betts, D. A. Young, D. D. Blankenship, J. L. Roberts, and M. J. Siegert (2016), The Australo-Antarctic Columbia to Gondwana transition, *Gondwana Res.*, *29*(1), 136–152, doi:10.1016/j.gr.2014.10.019.

Alley, R. B., D. D. Blankenship, and C. R. Bentley (1987), Till beneath ice stream B, *J. Geophys. Res.*, *92*(89), 8921–8929, doi:10.1029/JB092iB09p08921.

Alley, R., and D. Blankenship (1987), Till beneath ice stream B: 4. A coupled ice-till flow model, *J. Geophys. Res.*, *92*(B9), 8931–8940, doi:10.1029/JB092iB09p08931.

Bahr, D. B., E. W. H. Hutton, J. P. M. Syvitski, and L. F. Pratson (2001), Exponential approximations to compacted sediment porosity profiles, *Comput. Geosci.*, *27*(6), 691–700, doi:10.1016/S0098-3004(00)00140-0.

Bannister, S., J. Yu, B. Leitner, and B. L. N. Kennett (2003), Variations in crustal structure across the transition from West to East Antarctica, Southern Victoria Land, *Geophys. J. Intl.*, *155*, 870–884.

Baranov, A., and A. Morelli (2013), The Moho depth map of the Antarctica region, *Tectonophysics*, *609*(SI), 299–313, doi:10.1016/j.tecto.2012.12.023.

Blankenship, D., C. Bentley, S. T. Rooney, and R. B. Alley (1986), Seismic measurements reveal a saturated porous layer beneath an active Antarctic ice stream, *Nature*, *322*, 54–57.

Boger, S. (2011), Antarctica—Before and after Gondwana, *Gondwana Res.*, *19*(2), 335–371, doi:10.1016/j.gr.2010.09.003.

Carter, S. P., D. D. Blankenship, M. E. Peters, D. A. Young, J. W. Holt, and D. L. Morse (2007), Radar-based subglacial lake classification in Antarctica, *Geochem. Geophys. Geosyst.*, *8*, Q03016, doi:10.1029/2006GC001408.

Carter, S. P., D. D. Blankenship, D. A. Young, and J. W. Holt (2009), Using radar-sounding data to identify the distribution and sources of subglacial water: Application to Dome C, East Antarctica, *J. Glaciol.*, *55*(194), 1025–1040, doi:10.3189/002214309790794931.

Childers, V., R. Bell, and J. Brozena (1999), Airborne gravimetry: An investigation of filtering, *Geophysics*, *64*(1), 61–69.

Cook, C. P., et al. (2013), Dynamic behaviour of the East Antarctic ice sheet during Pliocene warmth, *Nat. Geosci.*, *6*(9), 765–769, doi:10.1038/ngeo1889.

Damaske, D., F. Ferraccioli, and E. Bozzo (2003), Aeromagnetic anomaly investigations along the Antarctic coast between Yule Bay and Mertz Glacier, *Terra Antart.*, *10*(3), 85–96.

Damiani, T. M., T. A. Jordan, F. Ferraccioli, D. A. Young, and D. D. Blankenship (2014), Variable crustal thickness beneath Thwaites Glacier revealed from airborne gravimetry, possible implications for geothermal heat flux in West Antarctica, *Earth Planet. Sci. Lett.*, *407*, 109–122, doi:10.1016/j.epsl.2014.09.023.

Drewry, D. J. (1976), Sedimentary basins of the East Antarctic Craton from geophysical evidence, *Tectonophysics*, *36*, 301–314.

Drewry, D. J. (1983), *Antarctica: Glaciological and Geophysical Folio*, Univ. Cambridge, Cambridge, U. K.

Fairhead, J. D., and C. S. Okereke (1988), Depths to major density contrasts beneath the West African rift system in Nigeria and Camaroon based on the spectral analysis of gravity data, *J. Afr. Earth Sci.*, *7*(5-6), 769–777.

Featherstone, W. E. (1995), On the use of Australian geodetic datums in gravity field determination, *Aust. J. Geod. Photogramm. Surv.*, *62*, 17–36, doi:10.1108/eb045337.

Ferraccioli, F., and E. Bozzo (1999), Inherited crustal features and tectonic blocks of the Transantarctic Mountains: An aeromagnetic perspective (Victoria Land, Antarctica), *J. Geophys. Res.*, *104*(B11), 25,225–297,319, doi:10.1029/1998JB900041.

Ferraccioli, F., F. Coren, and E. Bozzo (2001), Rifted (?) crust at the East Antarctic Craton margin: Gravity and magnetic interpretation along a traverse across the Wilkes Subglacial Basin region, *Earth Planet. Sci. Lett.*, *192*(3), 407–421.

Ferraccioli, F., P. C. Jones, A. P. M. Vaughan, and P. T. Leat (2006), New aerogeophysical view of the Antarctic Peninsula: More pieces, less puzzle, *Geophys. Res. Lett.*, *33*, L05310, doi:10.1029/2005GL024636.

Ferraccioli, F., E. Armadillo, T. Jordan, E. Bozzo, and H. Corr (2009), Aeromagnetic exploration over the East Antarctic Ice Sheet: A new view of the Wilkes Subglacial Basin, *Tectonophysics*, *478*(1–2), 62–77, doi:10.1016/j.tecto.2009.03.013.

Ferraccioli, F., C. Finn, and T. Jordan (2011), East Antarctic rifting triggers uplift of the Gamburtsev Mountains, *Nature*, *479*(7373), 388–92, doi:10.1038/nature10566.

Filina, I. Y., D. D. Blankenship, L. Roy, M. K. Sen, T. G. Richter, and J. W. Holt (2006), Inversion of airbourne gravity data over subglacial lakes East Antarctica, in *Antarctica: Contributions to Global Earth Science*, pp. 129–133, Springer, Berlin.

Filina, I., D. Blankenship, M. Thoma, V. V. Lukin, V. N. Masolov, and M. K. Sen (2008), New 3D bathymetry and sediment distribution in Lake Vostok: Implication for pre-glacial origin and numerical modeling of the internal processes within the lake, *Earth Planet. Sci. Lett.*, *276*(1–2), 106–114, doi:10.1016/j.epsl.2008.09.012.

Flottmann, T., G. M. Gibson, and G. Kleinschmidt (1993), Structural continuity of the Ross and Delamerian orogens of Antarctica and Australia along the margin of the paleo-Pacific, *Geology*, *21*, 319–322, doi:10.1130/0091-7613(1993)021<0319:SCOTRA>2.3.CO;2.

Fretwell, P., et al. (2013), Bedmap2: Improved ice bed, surface and thickness datasets for Antarctica, *Cryosphere*, *7*(1), 375–393, doi:10.5194/tc-7-375-2013.

Gibson, G. M., J. M. Totterdell, L. T. White, C. H. Mitchell, A. R. Stacey, M. P. Morse, and A. Whitaker (2013), Pre-existing basement structure and its influence on continental rifting and fracture zone development along Australia's southern rifted margin, *J. Geol. Soc.*, *170*(2), 365–377, doi:10.1144/jgs2012-040.

Gueguen, Y., and V. Palciauskas (1994), *Introduction to the Physics of Rocks*, Princeton Univ. Press, Princeton, N. J.

Holt, J. W., T. G. Richter, S. D. Kempf, D. L. Morse, and D. D. Blankenship (2006), Airborne gravity over Lake Vostok and adjacent highlands of East Antarctica, *Geochem. Geophys. Geosyst.*, *7*, Q11012, doi:10.1029/2005GC001177.

Jachens, R. C., and J. J. Griscom (1985), An isostatic residual gravity map of California, in *The Utility of Regional Gravity and Magnetic Anomaly Maps*, edited by W. J. Hinze, pp. 347–360, SEG Press, Tulsa, Okla.
Jamieson, S. S. R., and D. E. Sugden (2008), Landscape evolution of Antarctica, in *Antarctica: A Keystone in a Changing World—Online Proceedings for the Tenth International Symposium on Antarctica Earth Sciences*, edited by A. K. Cooper et al., pp. 39–54, Natl. Acad. Press, Washington, D. C.
Jamieson, S. S. R., N. R. J. Hulton, D. E. Sugden, A. J. Payne, and J. Taylor (2005), Cenozoic landscape evolution of the Lambert basin, East Antarctica: The relative role of rivers and ice sheets, *Global Planet. Change*, *45*(1–3), 35–49, doi:10.1016/j.gloplacha.2004.09.015.
Jamieson, S. S. R., D. E. Sugden, and N. R. J. Hulton (2010), The evolution of the subglacial landscape of Antarctica, *Earth Planet. Sci. Lett.*, *293*(1–2), 1–27, doi:10.1016/j.epsl.2010.02.012.
Jamieson, S. S. R., C. R. Stokes, and N. Ross (2014), The glacial geomorphology of the Antarctic ice-sheet bed, *Antart. Sci*, *26*(6), 1–38, doi:10.1017/S0954102014000212.
Jordan, T. A., F. Ferraccioli, E. Armadillo, and E. Bozzo (2013), Crustal architecture of the Wilkes Subglacial Basin in East Antarctica, as revealed from airborne gravity data, *Tectonophysics*, *585*, 196–206, doi:10.1016/j.tecto.2012.06.041.
Kane, M. F. (1962), A comprehensive system of terrain corrections using a digital computer, *Geophysics*, *27*(4), 455–462.
Karner, G. D., and A. B. Watts (1983), Gravity anomalies and flexure of the lithosphere at mountain ranges, *J. Geophys. Res.*, *88*(B12), 10,449–10,477, doi:10.1029/JB088iB12p10449.
Kilty, K. T. (1983), Werner deconvolution of profile potential field data, *Geophysics*, *1*(2), 234–237.
Krassay, A. A., D. L. Cathro, and D. J. Ryan (2004), A regional tectonostratigraphic framework for the Otway Basin, in *Eastern Australasian Basins Symposium II, Petroleum Exploration Society of Australia, Spec. Publ.*, edited by P. J. Boult, D. R. Johns, and S. C. Lang, pp. 97–116, PESA, Perth, Western Australia.
Ku, C. C., and J. A. Sharp (1983), Werner deconvolution for automated magnetic interpretation and its refinement using Marquardt's inverse modeling, *Geophysics*, *48*(6), 754–774, doi:10.1190/1.1441505.
LaFehr, T. R. (1991), An exact solution for the gravity curvature (Bullard B) correction, *Geophysics*, *56*(8), 1179–1184, doi:10.1190/1.1443138.
Laufer, A. L., G. Kleinschmidt, and F. Rossetti (2006), Late-Ross structures in the Wilson Terrane in the Rennick Glacier area, in *Antarctica—Contributions to Global Earth Sciences*, edited by D. K. Futterer et al., pp. 195–200, Springer, Berlin.
Lawrence, J. F., J. W. Van Wijk, and N. W. Driscoll (2007), Tectonic implications for the uplift of the Transantarctic Mountains *USGS Natl Acad. Ext. Abstr.*, 1–4.
Leao, J. W. D., P. T. L. Menezes, J. F. Beltrao, and J. B. C. Silva (1996), Gravity inversion of basement relief constrained by knowledge of depth at isolated points, *Geophysics*, *61*, 1702–1714.
Lloyd, A. J., A. A. Nyblade, D. A. Wiens, S. E. Hansen, M. Kanao, P. J. Shore, and D. Zhao (2013), Upper mantle seismic structure beneath central East Antarctica from body wave tomography: Implications for the origin of the Gamburtsev Subglacial Mountains, *Geochem. Geophys. Geosyst.*, *14*, 902–920, doi:10.1002/ggge.20098.
McMillan, M., H. Corr, A. Shepherd, A. Ridout, S. Laxon, and R. Cullen (2013), Three-dimensional mapping by CryoSat-2 of subglacial lake volume changes, *Geophys. Res. Lett.*, *40*, 4321–4327, doi:10.1002/grl.50689.
McNutt, M. K. (1983), Influence of plate subduction on isostatic compensation in Northern California, *Tectonics*, *2*(4), 399–415, doi:10.1029/TC002i004p00399.
Mengel, M., and A. Levermann (2014), Ice plug prevents irreversible discharge from East Antarctica, *Nat. Clim. Change*, *4*(6), 451–455, doi:10.1038/nclimate2226.
Ménot, R. P., G. Duclaux, J. J. Peucat, Y. Rolland, S. Guillot, M. Fanning, J. Bascou, D. Gapais, and A. Pêcher (2007), Geology of the Terre Adelie Craton, in *Antarctica: A Keystone in a Changing World—Online Proceedings for the Tenth International Symposium on Antarctica Earth Sciences*, *USGS Open File Rep.*, edited by A. K. Cooper and C. F. Raymond, 5 pp., U.S. Geol. Surv., Reston, Va.
Mercer, J. H. (1978), West Antarctic ice sheet and CO_2 greenhouse effect: A threat of disaster, *Nature*, *271*, 321–325.
Miller, K. G., J. D. Wright, J. V. Browning, A. Kulpecz, M. Kominz, T. R. Naish, B. S. Cramer, Y. Rosenthal, W. R. Peltier, and S. Sosdian (2012), High tide of the warm Pliocene: Implications of global sea level for Antarctic deglaciation, *Geology*, *40*(5), 407–410, doi:10.1130/G32869.1.
Minty, B. R. S. (1991), Simple micro-leveling for aeromagnetic data, *Explore Geophys.*, *22*, 591.
Nagy, D. (1966), The prism method for terrain corrections using digital computers, *Pure Appl. Geophys.*, *63*, 31–39.
Nyblade, A. A. (1999), Heat flow and the structure of Precambrian lithosphere, *Dev. Geotecton.*, *24*(C), 81–91, doi:10.1016/S0419-0254(99)80006-8.
Oldenburg, D. W. (1974), The inversion and interpretation of gravity anomalies, *Geophysics*, *39*(4), 526–536.
Parker, R. L. (1973), The rapid calculation of potential anomalies, *Geophys. J. R. Astron. Soc.*, *31*, 447–455.
Pollard, D., R. M. DeConto, and A. A. Nyblade (2005), Sensitivity of Cenozoic Antarctic ice sheet variations to geothermal heat flux, *Global Planet. Change*, *49*(1-2), 63–74, doi:10.1016/j.gloplacha.2005.05.003.
Pollard, D., R. M. DeConto, and R. B. Alley (2015), Potential Antarctic Ice Sheet retreat driven by hydrofracturing and ice cliff failure, *Earth Planet. Sci. Lett.*, *412*, 112–121, doi:10.1016/j.epsl.2014.12.035.
Regan, R., and W. Hinze (1976), The effect of finite data length in the spectral analysis of ideal gravity anomalies, *Geophysics*, *41*(1), 44–55.
Richter, T., J. Holt, and D. Blankenship (2001), Airborne gravity over East Antarctica, in *Proc Intl Symposium Kinematic Systems Geodesy, Geomatics, Navigation*, pp. 576–585, Dept. of Geomatics Engineering, Banff, Alberta, Canada.
Rippin, D. M., D. G. Vaughan, and H. F. J. Corr (2011), The basal roughness of Pine Island Glacier, West Antarctica, *J. Glaciol.*, *57*(201), 67–76, doi:10.3189/002214311795306574.
Roland, N. W. (1991), The boundary of the East Antarctic craton on the Pacific margin, in *Geological Evolution of Antarctica*, edited by M. R. A. Thomson, J. A. Crame, and J. W. Thomson, pp. 161–165, Cambridge Univ. Press, New York.
Rose, K. C., F. Ferraccioli, S. S. R. Jamieson, R. E. Bell, H. Corr, T. T. Creyts, D. Braaten, T. A. Jordan, P. T. Fretwell, and D. Damaske (2013), Early East Antarctic Ice Sheet growth recorded in the landscape of the Gamburtsev Subglacial Mountains, *Earth Planet. Sci. Lett.*, *375*, 1–12, doi:10.1016/j.epsl.2013.03.053.
Roy, L., M. Sen, D. Blankenship, P. Stoffa, and T. Richter (2005), Inversion and uncertainty estimation of gravity data using simulated annealing: An application over Lake Vostok, East Antarctica, *Geophysics*, *70*(1), 1–12.
Schroeder, D. M., D. D. Blankenship, and D. A. Young (2013), Evidence for a water system transition beneath Thwaites Glacier, West Antarctica, *Proc. Natl. Acad. Sci. U.S.A.*, *110*(30), 12,225–12,228, doi:10.1073/pnas.1302828110.
Schroeder, D. M., D. D. Blankenship, D. A. Young, A. E. Witus, and J. B. Anderson (2014), Airborne radar sounding evidence for deformable sediments and outcropping bedrock beneath Thwaites Glacier, West Antarctica, *Geophys. Res. Lett.*, *41*, 7200–7208, doi:10.1002/2014GL061645.Received.
Shepard, M. K., B. A. Campbell, M. H. Bulmer, T. G. Farr, L. R. Gaddis, and J. J. Plaut (2001), The roughness of natural terrain: A planetary and remote sensing perspective, *J. Geophys. Res.*, *106*(E12), 32,777–32,795, doi:10.1029/2000JE001429.

Siegert, M. J., and J. A. Dowdeswell (1996), Spatial variations in heat at the base of the Antarctic ice sheet from analysis of the thermal regime above subglacial lakes, *J. Glaciol.*, *42*, 501–509.
Smith, B. E., H. A. Fricker, I. R. Joughin, and S. Tulaczyk (2009), An inventory of active subglacial lakes in Antarctica detected by ICESat (2003–2008, *J. Glaciol.*, *55*(192), 573–595, doi:10.3189/002214309789470879.
Spector, A., and F. S. Grant (1970), Statistical models for interpreting aeromagnetic data, *Geophysics*, *35*, 293–302.
Steed, R. H. N. (1983), Structural interpretation of Wilkes Land, Antarctica, in *Antarctic Earth Science—Proc. Fourth Int. Symp. Antarct. Earth Sci*, edited by R. L. Oliver, P. R. James, and J. B. Jago, pp. 567–572, Cambridge Univ. Press, New York.
Stern, T. A., and U. S. ten Brink (1989), Flexural uplift of the Transantarctic Mountains, *J. Geophys. Res.*, *94*(2), 10,315–10,330, doi:10.1029/JB094iB08p10315.
Stern, T. A., A. K. Baxter, and P. J. Barrett (2005), Isostatic rebound due to glacial erosion within the Transantarctic Mountains, *Geology*, *33*(3), 221, doi:10.1130/G21068.1.
Studinger, M., R. E. Bell, W. R. Buck, G. D. Karner, and D. D. Blankenship (2004), Sub-ice geology inland of the Transantarctic Mountains in light of new aerogeophysical data, *Earth Planet. Sci. Lett.*, *220*(3–4), 391–408, doi:10.1016/S0012-821X(04)00066-4.
Sugden, D. E., D. R. Marchant, N. Potter Jr., R. A. Souchez, G. H. Denton, C. C. Swisher III, and J.-L. Tison (1995), Preservation of Miocene glacier ice in East Antarctica, *Nature*, *376*, 412–414.
Talwani, M., and M. Ewing (1960), Rapid computation of gravitational attraction of three-dimensional bodies of arbitrary shape, *Geophysics*, *25*, 203–225.
Taylor, J., M. J. Siegert, A. J. Payne, and B. Hubbard (2004), Regional-scale bed roughness beneath ice masses: Measurement and analysis, *Comput. Geosci.*, *30*, 899–908, doi:10.1016/j.cageo.2004.06.007.
ten Brink, U., and T. A. Stern (1992), Rift flank uplifts and hinterland comparison of the Transantarctic Mountains with the Great Escarpment of Southern Africa, *J. Geophys. Res.*, *97*(B1), 569–585, doi:10.1029/91JB02231.
Watson, D. (1992), *Contouring: A Guide to the Analysis and Display of Spatial Data*, Pergamon, Turkey.
Watts, A. (2001), *Isostasy and Flexure of the Lithosphere*, Cambridge Univ. Press, Cambridge, U. K.
Wessel, P., and W. H. F. Smith (1998), New, improved version of generic mapping tools released, *Eos, Trans. AGU*, *79*, 579–579, doi:10.1029/98EO00426.
White, L. T., G. M. Gibson, and G. S. Lister (2013), A reassessment of paleogeographic reconstructions of eastern Gondwana: Bringing geology back into the equation, *Gondwana Res.*, *24*(3–4), 984–998, doi:10.1016/j.gr.2013.06.009.
Wilson, D. S., S. S. R. Jamieson, P. J. Barrett, G. Leitchenkov, K. Gohl, and R. D. Larter (2012), Antarctic topography at the Eocene-Oligocene boundary, *Palaeogeogr. Palaeoclimatol. Palaeoecol.*, *335–336*, 24–34, doi:10.1016/j.palaeo.2011.05.028.
Wingham, D. J., M. J. Siegert, A. Shepherd, and A. S. Muir (2006), Rapid discharge connects Antarctic subglacial lakes, *Nature*, *440*(7087), 1033–1036, doi:10.1038/nature04660.
Wright, A., and M. Siegert (2012), A fourth inventory of Antarctic subglacial lakes, *Antarct. Sci.*, *24*(06), 659–664, doi:10.1017/S095410201200048X.
Wright, A. P., et al. (2012), Evidence of a hydrological connection between the ice divide and ice sheet margin in the Aurora Subglacial Basin, East Antarctica, *J. Geophys. Res.*, *117*, F01033, doi:10.1029/2011JF002066.
Wright, A. P., D. A. Young, J. L. Bamber, J. A. Dowdeswell, A. J. Payne, D. D. Blankenship, and M. J. Siegert (2014), Subglacial hydrological connectivity within the Byrd Glacier catchment, East Antarctica, *J. Glaciol.*, *60*(220), 345–352, doi:10.3189/2014JoG13J014.
Young, D. A., et al. (2011), A dynamic early East Antarctic Ice Sheet suggested by ice-covered fjord landscapes, *Nature*, *474*(7349), 72–5, doi:10.1038/nature10114.
Zoback, M. D. (2010), *Reservoir Geomechanics*, Cambridge Univ. Press, Cambridge, U. K.